Thin-Film Electroluminescent Device Physics Modeling

J. C. Hitt, J. P. Bender, and J. F. Wager[1]
Department of Electrical and Computer Engineering
Center for Advanced Materials Research
Oregon State University, Corvallis, OR 97331–3211

ABSTRACT: Previous and current approaches to alternating current thin-film electroluminescent (ACTFEL) device physics modeling are reviewed. The primary goal of the modeling efforts of interest to this review is to accurately simulate the electrical properties of two-terminal ACTFEL test structures when subjected to realistic applied voltage waveforms. A comprehensive review of previous ACTFEL modeling efforts is presented. Additionally, two modeling methodologies that are believed to hold the most promise for accurate ACTFEL device modeling are presented. These methodologies involve state-space simulation of a discretized phosphor and SPICE simulation.

Table of Contents

I. Introduction

Alternating current thin-film electroluminescent (ACTFEL) devices are currently employed in commercial monochrome and multicolor flat-panel displays [1, 2]. Key advantages of ACTFEL displays

[1]Corresponding author: email: jfw@ece.orst.edu

1040-8436/00/$.50

are broad operating temperature, ruggedness, long-lifetime, and wide viewing angle. ACTFEL displays are an appropriate choice for a wide variety of military, automotive, industrial, and medical applications in which the best attributes of ACTFEL technology are highly valued. ACTFEL technology is under development for full-color and miniature displays, as well as for hard-copy and other light source applications.

An ACTFEL device is a thin-film stack, typically consisting of a phosphor layer doped with a luminescent impurity (e.g., ZnS:Mn, SrS:Cu, etc.) which is sandwiched between two insulators that are in turn contacted by an opaque and a transparent electrode. Usually an ACTFEL stack is deposited onto a glass substrate with the transparent conductor as the bottom electrode so that light is viewed through the substrate glass. However, inverted structures are sometimes used, in which case the electrodes are reversed and light is viewed from the top side of the device.

Note that an ACTFEL device involves capacitive coupling between the electrodes and the phosphor. Capacitive coupling necessitates the use of alternating current (AC) voltage waveform excitation which is applied between the two contacts to induce light emission.

The six basic physical processes responsible for ACTFEL operation are illustrated in Fig. 1 and are summarized as follows.

1. Injection — When an adequately large voltage is applied to the ACTFEL device, the phosphor field at the cathode phosphor/insulator interface is large enough that trapped interface state electrons are tunnel-emitted into the phosphor conduction band. It is possible that some of these conduction band electrons are injected from bulk trap states; this is not shown in Fig. 1 and would lead to the formation of space charge in the phosphor and a concomitant nonuniform field across the phosphor which would manifest itself in Fig. 1 as a phosphor energy band whose slope decreases in magnitude across the phosphor from the cathode to the anode phosphor/insulator interface.

2. Transport — Electrons injected into the phosphor conduction band gain energy from the electric field and are transported across the phosphor. Although it is not shown in Fig. 1, it is possible that some of these transported electrons become sufficiently heated to induce electron multiplication in the phosphor via trap-to-band or band-to-band impact ionization. Both band-to-band impact ionization (with hole trapping in bulk trap states) and trap-to-band impact ionization result in the creation of space charge in the phosphor, again which would lead to curvature in the phosphor energy bands.

3. Impact excitation — As hot electrons transit the phosphor, a fraction of them excite luminescent impurities from their ground state (G) to their excited state (E).

4. Radiative recombination — Relaxation of the electron from its excited state back to its ground state ideally results in photon emission, although this process could also occur nonradiactively.

5. Electron trapping — Transported electrons reach the phosphor/insulator interface where they are trapped. Usually this trapping is presumed to occur at interface states, but in certain situations some of this trapping may occur in bulk states near the anode phosphor/insulator interface.

6. Optical outcoupling — Photons generated via radiative recombination of luminescent impurities outcouple from the ACTFEL stack and are observed by the viewer.

The purpose of this article is to review previous and current approaches to ACTFEL device physics modeling. More specifically, the primary aim of the modeling efforts of interest to this review is to accurately simulate the electrical properties of two-terminal ACTFEL test dot structures when subjected to realistic applied voltage waveforms. Thus, in the context of the six physical processes previously enumerated, the focus of this review is with respect to Process 1, part of 2, and 5. More precisely, the primary physical processes necessary to simulate are: injection (from

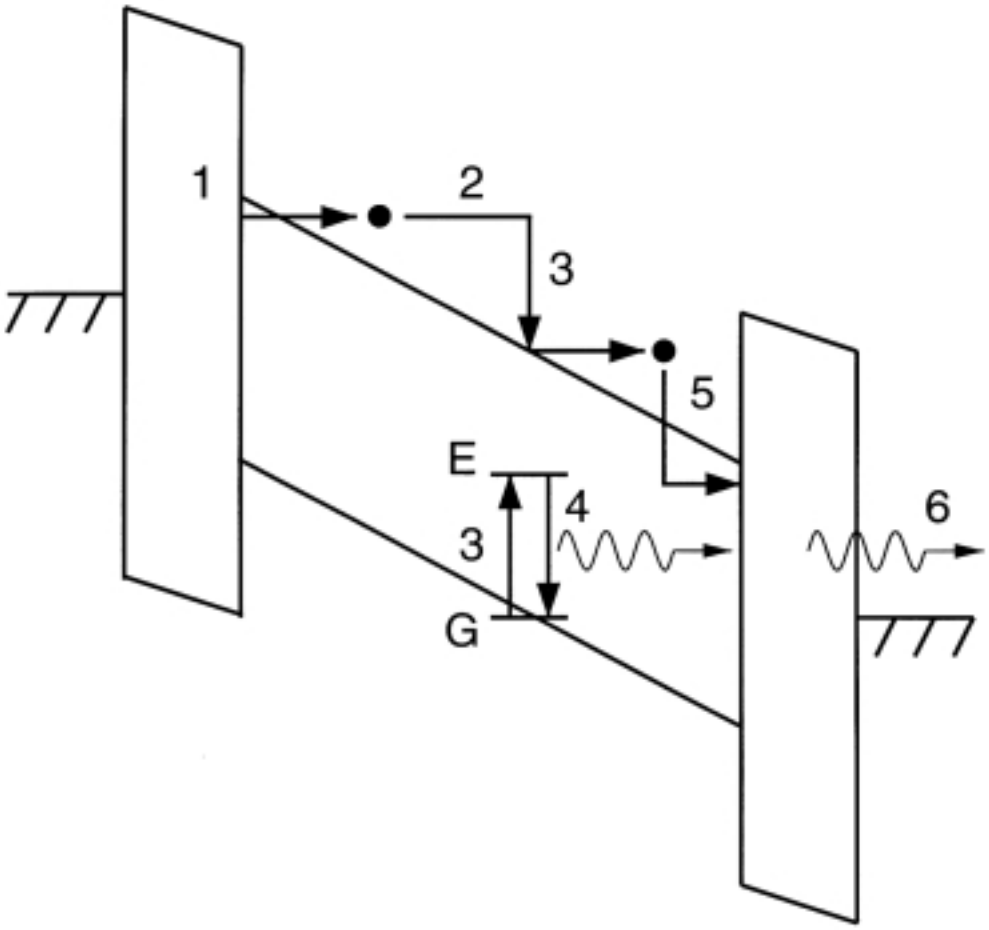

Figure 1: Energy band diagram illustrating the six primary physical processes responsible for ACTFEL operation.

interface and bulk traps), trap-to-band impact ionization, band-to-band impact ionization and hole trapping, and electron trapping (to both interface and bulk traps). To the uninitiated, this goal may seem a bit puzzling since all of the optical phenomena from which ACTFEL displays derive their utility are omitted from consideration. However, it is our experience that the most difficult aspect of ACTFEL device modeling, by far, is accurately accounting for measured electrical trends when ACTFEL devices are subjected to realistic waveforms. Indeed, although much progress has been made with respect to ACTFEL device physics modeling of electrical trends, this review will show that this objective has not yet been met and is the topic of ongoing research.

This review is divided into two primary sections involving previous and current modeling activities. The first section is an attempt to survey previous ACTFEL device physics modeling work. It is hoped that this overview will provide most of the references necessary for someone beginning a study of this topic and wanting to know what has been accomplished previously. The second section focuses on modeling methodologies that we believe have the most potential to reach the

goal of providing accurate two-terminal simulation of ACTFEL test structures subjected to realistic applied waveforms. Note that both sections of the review are further sub-divided into two categories, device physics and SPICE modeling. In our experience, concurrent development of device physics and SPICE models is desirable because of the synergy between these two modeling methodologies. Moreover, each modeling approach is more suitable for a given situation.

Finally, to end this introductory section, it is appropriate to specify what this review does not address. First, it does not address the primarily optical aspects of ACTFEL behavior; namely, impact excitation (Process 3) [3, 4, 5, 6], radiative recombination (Process 4) [2, 5, 7], or optical outcoupling (Process 6) [8]. Also, the high-field transport issues determining the hot electron distribution (e.g., band structure, scattering mechanisms, collision broadening, etc.) are not addressed in this review [5, 6, 9, 10]. Additionally, this review does not include a discussion of issues relevant to modeling passive- or active-matrix displays (e.g., distributed RC networks, driver electronics modeling, luminance and power performance of displays, etc.) [11, 12, 13].

II. Previous Actfel Modeling

A. Device Physics Modeling

The first effort to model an ACTFEL device appears to have been undertaken by Chen and Krupka [14] in conjunction with their introduction of several novel ACTFEL characterization methods. Although their ACTFEL devices had only a single insulator, most of their characterization and analysis results are relevant to modern dual-insulator ACTFEL devices. Their modeling approach involved writing device physics equations for the instantaneous field across and current through the phosphor layer in terms of the externally measured voltage and current. The main aim of their work was to demonstrate new ACTFEL characterization methods and to provide evidence for field-clamping, in which the phosphor field remains approximately constant for applied voltages above threshold. Additionally, Chen and Krupka proposed the first equivalent circuit for an ACTFEL device, as shown in Fig. 2, in which the insulator is represented by a capacitor and the phosphor is modeled as a parallel combination of a capacitor and a nonlinear voltage-dependent resistor to represent conduction across the phosphor.

An early ACTFEL device physics modeling overview was provided by Smith [15]. He proposed the ACTFEL equivalent circuit shown in Fig. 3 in which the phosphor is represented as a capacitor shunted by two back-to-back Zener diodes to account for conduction in the phosphor. Additionally, Smith employed the field-clamping model of Chen and Krupka and quantified the emission rate from interface states as a function of phosphor field by assuming that tunneling occurs from a Dirac well. Smith also discussed the effect of space charge in modifying the "band bending," and thus affecting electron transport. Moreover, he enumerated field ionization, trap-to-band impact ionization, band-to-band impact ionization, trap capture, and Auger recombination as physical processes likely to be of importance in the generation of space charge.

One of the most sophisticated ACTFEL device physics models ever developed was reported by Howard, Sahni, and Alt [16]. Although their intent was to model hysteretic properties of the luminance-voltage (L-V) characteristics of ACTFEL devices, most of their development is relevant to modern, non-hysteretic devices. Their formulation consists of analytical expressions for tunnel injection from a discrete interface state modeled as a Coulombic well, continuity equations for electrons and holes in which band-to-band impact ionization is included, and use of the Poisson

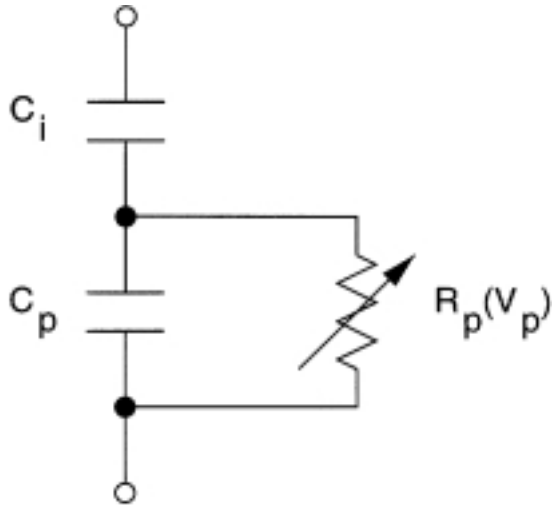

Figure 2: Chen and Krupka's equivalent circuit for an ACTFEL device. The insulator is represented as a capacitor. The phosphor is represented as a capacitor shunted by a nonlinear voltage-dependent resistor to represent conduction current through the phosphor.

equation to evaluate the local phosphor field subject to a time-dependent voltage boundary condition. This formulation leads to a set of six coupled equations that must be solved numerically in a self-consistent manner. One of the primary conclusions of their study is that bistability in an ACTFEL device, and hence L-V hysteresis, requires a deep hole trap concentration of 10^{16} to 10^{17} cm^{-3} and that these hole traps must have a sufficiently large capture cross-section so that they can be efficiently neutralized via electron capture.

In an early ACTFEL review article, Alt presents a very simple, but useful, "ideal model" for the ACTFEL device [17]. This model assumes that the phosphor layer can be modeled (Fig. 4) as a capacitor shunted by a voltage-controlled current source which turns on abruptly and strongly at the threshold voltage. This model corresponds to assuming that ideal field-clamping occurs. The only parameter for this model is the threshold voltage. This "ideal model" is often employed to estimate the transferred charge and luminance expected for an ACTFEL device at a given overvoltage (i.e., the applied voltage in excess of the threshold voltage). Alt also discusses a "nearly ideal model," which involves setting up and numerically integrating a differential equation for charge transfer and yields a dynamic description of the phosphor field, charge, and current. Steady-state solutions may also be obtained from the "nearly ideal model" by integrating over several periods of the applied voltage waveform.

Bringuier refined and extended the "nearly ideal model" in several important ways [5, 18, 19]. First, he derived the dynamical equations defining ACTFEL operation for a device with no space charge present in the phosphor and with either a discrete or distributed interface state distribution [18]. Second, he developed the solutions to these dynamic equations, presented approximate solutions, and discussed implications of these solutions. For the distributed interface state problem, he outlined the solution to the most general dynamic equation and he also presented a more simplified solution involving an assumption of quasi-equilibrium and the use of the quasi-Fermi level. He then showed useful simulation examples of the transient behavior of the phosphor field, the quasi-Fermi level,

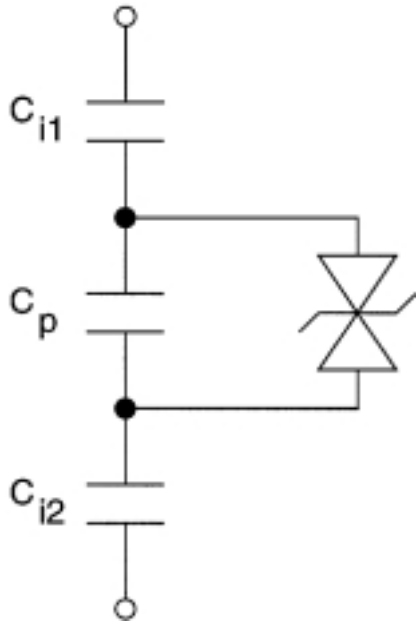

Figure 3: Smith's equivalent circuit for an ACTFEL device. Insulators are represented as capacitors. The phosphor is represented as a capacitor shunted by two back-to-back Zener diodes to account for conduction in the phosphor. The threshold voltage is set by the breakdown voltage of the Zener diodes and the abruptness of the turn-on may be controlled by the series resistance of the Zener diodes.

and the current when an ACTFEL device with distributed interface states is subjected to sinusoidal or pulse voltage waveform excitation. Third, he extended the model to include band-to-band impact ionization, developing the necessary dynamic equations in the framework of the quasi-Fermi level approximation. [19] An important aspect of this work was his recognition of the importance of the hole recombination rate and how a slow rate of hole recombination can affect the shape of measured transferred charge characteristics. Bringuier's ACTFEL device physics modeling is perhaps the most lucid and thoughtful work yet reported.

Ylilammi proposed the ACTFEL equivalent circuit shown in Fig. 5 [20]. Note that the two insulators have been combined in series and lumped together. In contrast to most ACTFEL equivalent circuit models, the phosphor capacitance is shunted by two branches, each of which accounts for the flow of charge in one direction. Each shunt branch is comprised of two resistors, one diode, and one Zener diode; the model parameters of each of these branches are identical for symmetric ACTFEL devices but differ for asymmetrical devices. For sinusoidal voltage excitation, an exact analytical solution is obtained for the device current, transferred charge, and internal voltage across the phosphor. For more complicated applied voltage waveforms, a numerical solution is preferred.

Much of the following discussion regards space charge, a topic that requires some preliminary discussion prior to reviewing space charge modeling. Various workers have discussed space charge characterization [21, 22, 23, 24, 25, 26, 27, 28, 29, 30, 31, 32, 33, 34, 35, 36, 37, 38, 39, 40, 41] and modeling [28, 34, 36, 42, 43, 44, 45, 46, 47, 48, 49, 50, 51, 52, 53].

For the purpose of this review, we will distinguish three kinds of space charge: (1) fixed, (2) static,

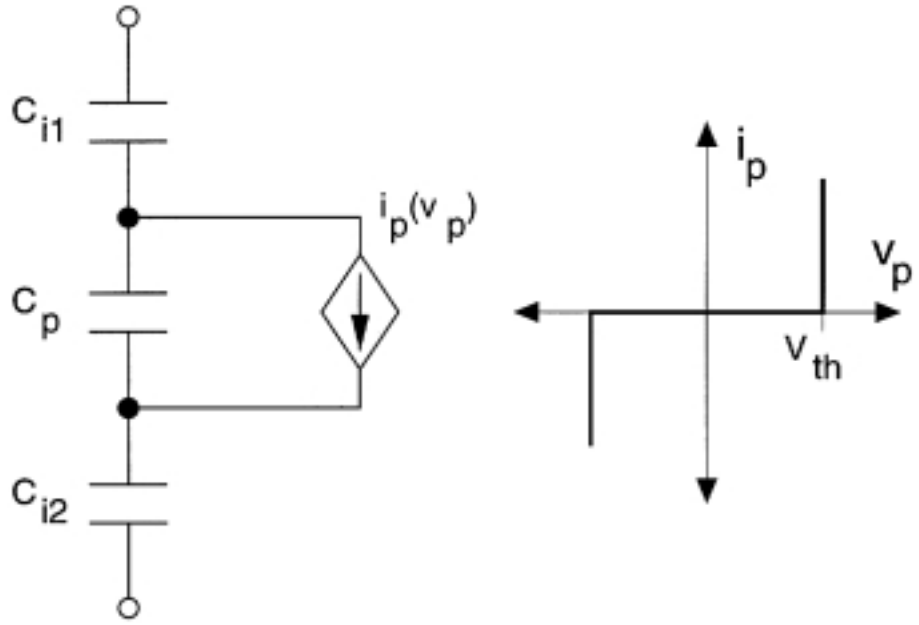

Figure 4: Alt's equivalent circuit for an ACTFEL device. Insulators are represented as capacitors. The phosphor is represented as a capacitor shunted by a voltage-controlled current source to represent conduction current through the phosphor. Alt's "ideal model" corresponds to assuming that the current source turns-on strongly and abruptly at the threshold voltage, as shown in the i_p-v_p curve. Less ideal, more realistic models would account for the nonlinear i_p-v_p relationship of the voltage-controlled current source.

and (3) dynamic. Fixed space charge refers to a situation in which net charge exists within the phosphor and which is always present in the same concentration, independent of whether or not a voltage is applied to the ACTFEL device. Note that charge neutrality for such a situation implies that this omnipresent charge is balanced by an equal amount of charge of opposite polarity somewhere within the ACTFEL device (i.e., most likely at the phosphor/insulator interfaces). Static space charge refers to charge that exists within the phosphor in an essentially steady-state manner during AC voltage excitation of the ACTFEL device. The idea of static space charge is that this charge somehow builds up during ACTFEL device operation and its time constant for annihilation is slow enough that it establishes a steady-state density. Thus, the annihilation time constant for this kind of charge is significantly longer than the period of the applied voltage waveform. This kind of space charge and its designation as "static" has often puzzled ACTFEL researchers when they encounter it for the first time. In retrospect, denoting it as "steady-state space charge" would be less confusing. However, this terminology seems to be established in the ACTFEL literature so that we will persist in using the term static to denote this type of space charge. Note that the clearest way to distinguish static and dynamic space charge is via device physics simulation, as presented in Section 3.1. Dynamic space charge denotes space charge that is both created and annihilated in times less than one period of the applied voltage waveform.

Of the three kinds of space charge, most workers have been concerned primarily with dynamic space charge since it is most noticeable in affecting the electrical and electro-optic properties of

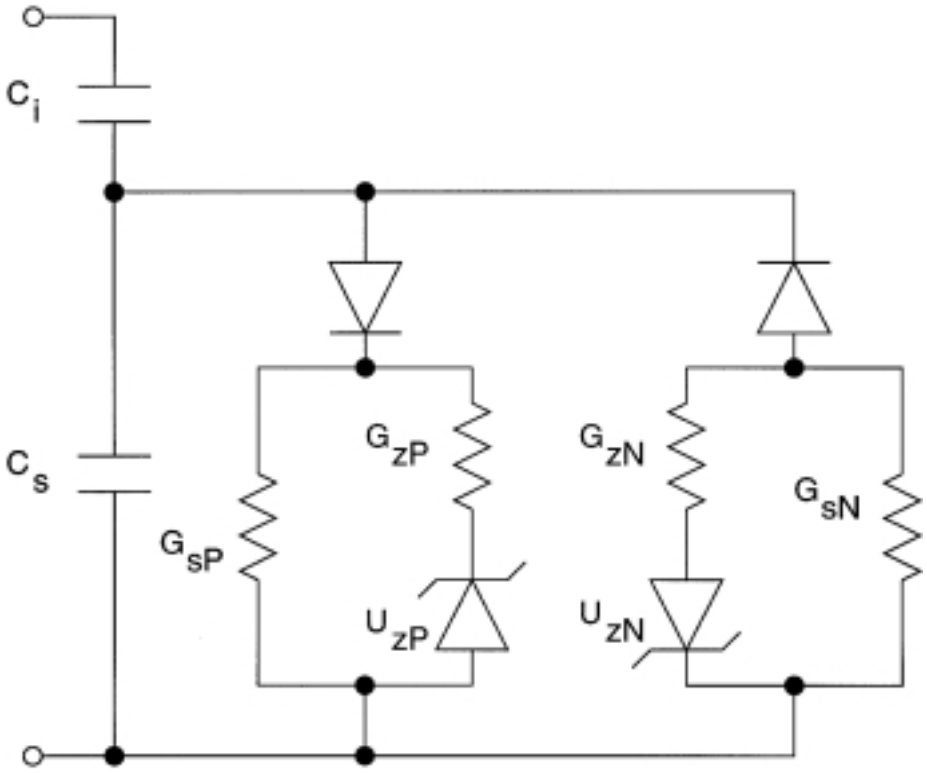

Figure 5: Ylilammi's equivalent circuit for an ACTFEL device. The two insulators are represented as capacitors that have been combined in series and lumped together. The phosphor capacitance is shunted by two branches, each of which accounts for the flow of charge in one direction. Each shunt branch is comprised of two resistors, one diode, and one Zener diode; the model parameters of each of these branches are identical for symmetric ACTFEL devices but differ for asymmetrical devices.

ACTFEL devices. More recently, the role of static space charge has been appreciated, but this kind of space charge manifests itself in less obvious ways. Fixed space charge has been discussed infrequently. Also, note that, with very few exceptions, phosphor space charge is implicitly assumed to involve positive charge. Positive space charge is expected since electrons are the dominant carriers in ACTFEL devices and it is unlikely that many electron traps in the phosphor will remain filled with electrons under the high-fields at which ACTFEL devices operate.

Experimentally, we distinguish between dynamic and static space charge in the following manner [39]. Dynamic space charge manifests itself as overshoot in capacitance-voltage (C-V) or internal charge-phosphor field (Q-F_p) characteristics. Thus, when an ACTFEL device exhibits C-V or Q-F_p overshoot, dynamic space charge is present in the device. From a comparative point-of-view, for two similar ACTFEL devices (i.e., with similar phosphor thicknesses and insulating layers) measured in the same manner (i.e., using the same test set-up and applied voltage waveform with the same overvoltage), the one with the larger overshoot has more dynamic space charge. Static space charge is more difficult to experimentally assess. We have found that overshoot in transferred charge capacitance curves can arise from either static or dynamic overshoot. Thus, when dynamic

space charge is not present in an ACTFEL device, the existence of overshoot in transferred charge capacitance is evidence for static space charge. Although this is the case for evaporated ZnS:Mn ACTFEL devices, it is our experience that most ACTFEL devices exhibit both dynamic and static space charge; in such situations, it is difficult to unequivocally distinguish static from dynamic space charge.

Given these space charge remarks, the overview of previous ACTFEL device physics modeling can be continued.

Singh et al. were among the first to recognize the important role played by space charge in determining the operation of ACTFEL devices and to attempt to model such effects [22, 44, 46]. Their primary procedure for experimentally monitoring the presence of space charge was to observe trailing edge luminescence from ACTFEL devices subjected to various kinds of pulsed voltage excitation. Subsequently, they developed a model to account for trailing edge emission in both ZnS:Mn and SrS:Ce ACTFEL devices. This model involved discretization of the phosphor; interface state tunnel injection from one or more discrete interface states; interaction of phosphor conduction band electrons with one or more discrete traps via tunnel emission, thermal emission, or recombination; modeling of impact excitation of luminescent impurities; modeling interfacial electron capture as a boundary condition; and modeling of the luminescent response from the impact excitation rate. One of the primary results of their modeling effort is that trailing edge emission can be simulated through the inclusion of a second, more shallow interface state level.

Neyts et al. have undertaken several types of ACTFEL device physics modeling studies [28, 36, 42, 43, 51]. One aspect of their work involved using a simplified version of the tunneling rate expression so that analytical steady-state solutions to ACTFEL devices without space charge could be obtained [42]. Other work involved using analytical simplifications to the device physics equations in order to assess hysteresis and dynamic space charge in ZnS:Mn and SrS:Ce ACTFEL devices. Both trailing edge emission, associated with dynamic space charge, and negative resistance, a necessary requirement for hysteresis, could be realistically simulated using this approach.

Keir et al. employed sheet charge modeling to account for dynamic space charge in ACTFEL devices [34, 47, 48, 49]. The idea of sheet charge modeling is to approximate the actual space charge distribution by one or more sheets which represent the local space charge centroid. A single-sheet space charge model was developed in which space charge creation is assumed to occur either by field-aided emission from bulk traps or by trap-to-band impact ionization. Simulation showed that either space-charge creation mechanism could give rise to asymmetrical C-V and Q-F_p overshoot, as experimentally observed in atomic layer epitaxy (ALE) ZnS:Mn ACTFEL devices. Also, simulation clarified that overshoot is more pronounced when space charge is created nearer to the interface from which electrons are sourced. Moreover, analysis demonstrated that capacitance or transient current overshoot is a consequence of having electron multiplication occur within the phosphor layer; analytical expressions were obtained for the transient current and capacitance, which included the effect of electron multiplication in terms of the single-sheet charge model. Use of the single-sheet space charge model provided analytical clarification of how dynamic space charge distorts the shape of a Q-F_p curve. One application of the single-sheet space charge model involved simulating the effects of offset in Q-V and Q-F_p curves [50]; offset is discussed further in Section 3.1. Finally, two different equivalent circuits were deduced for the single-sheet space charge model, depending on whether space charge generation occurs via field-aided bulk trap emission or trap-to-band impact ionization; a discussion of these equivalent circuits is postponed until Section 2.2.

Keir also developed a two-sheet space charge model so that concomitant creation and annihi-

lation of dynamic space charge could be simulated [48]. This situation is appropriate for SrS:Ce ACTFEL device operation in which space charge is created in the high-field region near the cathode insulator/phosphor interface and electrons radiatively recombine in the low-field region near the anode insulator/phosphor interface. In Keir's version of the two-sheet space charge model, space charge creation is only modeled for field-aided emission from bulk traps.

Recently, the two-sheet space charge model of Keir has been employed for simulation and has been extended to include trap-to-band impact ionization [52, 53]. First, it has been employed to simulate the C-V and Q-F_p characteristics of SrS:Ce ACTFEL devices [52]. Keir's two-sheet charge model, in which space charge generation is presumed to occur via field-assisted emission of bulk traps, is found to yield good agreement between simulated and measured conduction charge, leakage charge, relaxation charge, polarization charge, and steady-state phosphor field. However, this two-sheet space charge model fails to explain the large experimental C-V or Q-F_p overshoot or the experimental turn-on voltage trends observed in SrS:Ce ACTFEL devices. This disagreement between experiment and simulation is attributed to the use of an inappropriate space charge creation mechanism, field-assisted emission of bulk traps. Second, the two-sheet space charge model was extended to include dynamic space charge creation via trap-to-band impact ionization [53]. This model leads to substantially more C-V and Q-F_p overshoot than when space charge creation occurs via field-ionization of bulk traps; however, it is important to note that this overshoot enhancement is significant only if the effects of the test circuit series resistance are included in the simulation. This result underscores the importance of including relevant test circuit elements in the simulation. In general, we have not been able to accurately simulate ACTFEL device experimental electrical characteristics unless test circuit elements are included in the simulation. Since it is a nontrivial task to include the effects of even a simple test circuit resistor into a device physics-based simulation, our preference is to employ either state-space or SPICE methods in future ACTFEL modeling endeavors since it is very easy to include test circuit elements using these modeling methodologies.

A simple state-space model was developed by Peery in an attempt to perform a realistic simulation of the steady-state electrical characteristics of evaporated ZnS:Mn ACTFEL devices [54]. A detailed description of state-space modeling and its advantages is presented in Section 3.1. Briefly, Peery's state-space model accounted for certain test circuit elements (i.e., the series resistor and the sense capacitor) and the ACTFEL phosphor is modeled as a single capacitor shunted by a nonlinear, voltage-controlled current source. Two primary conclusions resulted from this work. First, much effort was expended to try to account for experimental leakage charge and turn-on voltage trends through the inclusion of a distributed interface state density, but no bulk space charge. It was found that no realistic, or even unrealistic distribution of interface states could provide simulations that would simultaneously account for experimental leakage charge and turn-on voltage trends. Thus, the steady-state electrical characteristics of evaporated ZnS:Mn ACTFEL devices cannot be ascribed to a purely interfacial model. Second, much more promising simulation results were obtained when holes were included via band-to-band impact ionization and hole trapping. Moreover, simulation indicates that it is essential to include hole re-emission from bulk traps in this simulation in order to account for both leakage and relaxation charge trends. However, even though Peery's modeling study was able to discount the need for distributed interface states and to underscore the importance of holes in determining experimental electrical trends, his state-space formulation was determined to be inadequate since it is impossible to simulate dynamic space charge effects, such as C-V and Q-F_p overshoot, when the phosphor is modeled as a single layer. This insight provided some of the impetus for the development of the n-sheet, state-space model, as described in Section 3.1.

B. SPICE Modeling

SPICE (simulation program with integrated circuit emphasis) is a computer-aided design circuit simulator. We have found SPICE analysis to be a complementary path for undertaking ACTFEL device physics modeling. There are two main ways that SPICE analysis may be employed in this regard.

First, as evident from the discussion of Section 2.1, most ACTFEL model development begins with the formulation of an equivalent circuit to represent the ACTFEL device. SPICE is useful for simulating ACTFEL equivalent circuit models, particularly if these models are comprised of conventional circuit elements (e.g., resistors, capacitors, diodes, etc.) for which SPICE models already exist. Both the transient and steady-state response of an ACTFEL device subjected to a simple or a very complicated applied voltage waveform may be readily obtained via SPICE analysis. Also, test circuit elements can be easily incorporated into the simulation. We have found this first way of employing SPICE analysis to be very useful for testing hypotheses regarding the interpretation of measured experimental trends and regarding the viability of certain aspects of device physics models under consideration.

Second, once a new device physics model has been constructed, it is possible to develop a corresponding SPICE device model by mapping the device physics model equations into an appropriate equivalent circuit. This device-physics-equations-to-SPICE-model mapping is facilitated by the use of energy band diagrams. Often, the device physics equations are represented by some type of nonlinear, controlled source and constitute the defining equations for this controlled source. An example of this second way of using SPICE is given in Section 3.2. Note that this second way of using SPICE is actually the conventional way in which SPICE is used; i.e., first SPICE models are developed from device physics equations, then circuit and systems designers employ these SPICE models for analysis and design. Thus, the first way in which SPICE is used as a device physics model building tool is rather unconventional.

The first ACTFEL SPICE modeling effort was reported by Davidson et al. [56, 57], in which experimental and SPICE-simulated C-V characteristics of evaporated ZnS:Mn ACTFEL devices are compared. Davidson's equivalent circuit is shown in Fig. 6. R_{ITO} is a lumped resistor accounting for the non-zero series resistance of the ITO electrode. The phosphor is represented as a capacitor shunted by R_p, a parallel resistance accounting for DC leakage, and a series combination of back-to-back Zener diodes and a resistor R_d. The physical nature of R_d is uncertain, but inclusion of this resistor led to improved simulation results. SPICE simulation of parametric variations of model parameters was found to be useful in interpreting measured C-V trends.

Douglas and Wager [58, 59, 60] refined Davidson's equivalent circuit and developed an optical SPICE model to account for luminance trends in evaporated ZnS:Mn ACTFEL devices. Douglas's equivalent circuit is shown in Fig. 7. Note that this equivalent circuit is identical to Davidson's except that a parallel RC network is inserted in the back-to-back Zener diode shunt path. Inclusion of this parallel RC network was found to be necessary in order to account for the applied voltage waveform dependence of the turn-on voltage and relaxation charge, and for transient phosphor field trends. The physical origin of this parallel RC network is not entirely clear; perhaps it is associated with hole re-emission from bulk trap states. Douglas also developed an optical SPICE model, which is shown in Fig. 8. The purpose of the optical SPICE model is to account for transient luminance [L(t)] and luminance-voltage [L-V] trends. The current source driving the RC network arises from the instantaneous conduction current simulated using Douglas' equivalent circuit ACTFEL model (Fig. 7). The two parallel RC branches account for two decay time constants. The instantaneous

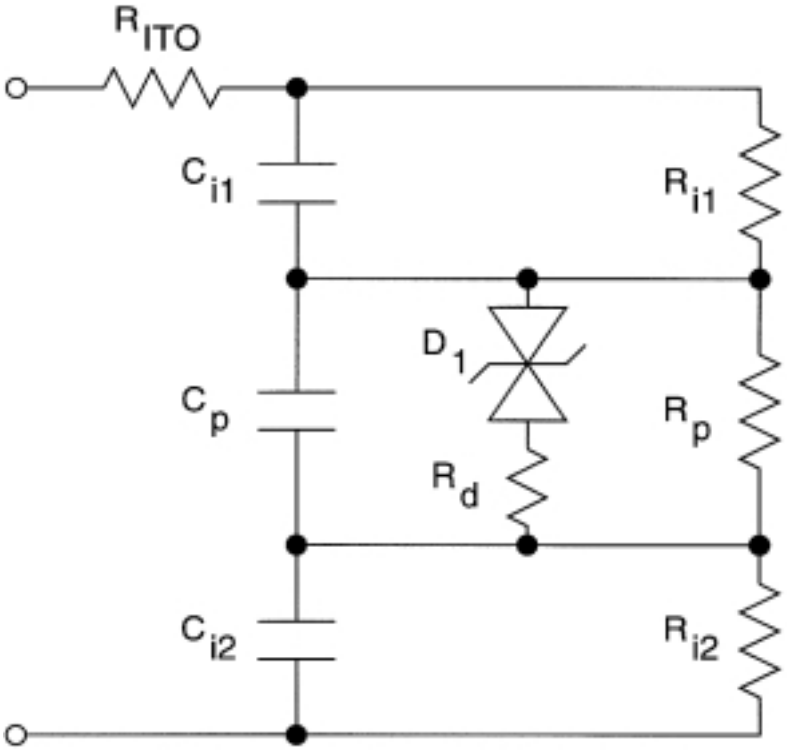

Figure 6: Davidson's equivalent circuit for an ACTFEL device. Each insulator is represented as a capacitor shunted by a resistor which accounts for DC leakage. R_{ITO} is a lumped resistor accounting for the non-zero series resistance of the ITO electrode. The phosphor is represented as a capacitor shunted by R_p, a parallel resistance accounting for DC leakage, and a series combination of back-to-back Zener diodes and a resistor R_d. The physical nature of R_d is uncertain, but inclusion of this resistor led to improved simulation results.

luminance of the ACTFEL device is taken as proportional to the current through the shunt resistor, R_3. The optical SPICE model was shown to reproduce measured L(t) and L-V trends quite closely.

An ACTFEL equivalent circuit model investigated by Åberg for the simulation of passive matrix EL displays is shown in Fig. 9. [11] Åberg considers three different variations of this circuit, depending on whether the impedance labeled "X" in Fig. 9 consists of (1) a resistor, (2) a resistor and capacitor in series, or (3) an inductor. Åberg uses circuit (1) to simulate ALE ZnS:Mn ACTFEL devices which do not exhibit L-V hysteresis. In contrast, he shows that model (2) can be used to simulate ACTFEL devices which exhibit L-V hysteresis. Model (3) is proposed as one way to account for dynamic space charge generation. He points out that capacitance overshoot associated with dynamic space charge may be interpreted as arising from a negative phosphor capacitance; note that the positive reactance associated with the inductor of version (3) of the circuit shown in Fig. 9 is equivalent to a negative capacitance. Alternatively, Åberg also proposes the switched capacitor model shown in Fig. 10 to account for capacitance overshoot due to dynamic space charge generation; the switch shown in Fig. 10 is closed during an applied voltage pulse and is open between voltage pulses. Åberg finds that dynamic space charge effects may be more accurately simulated using the

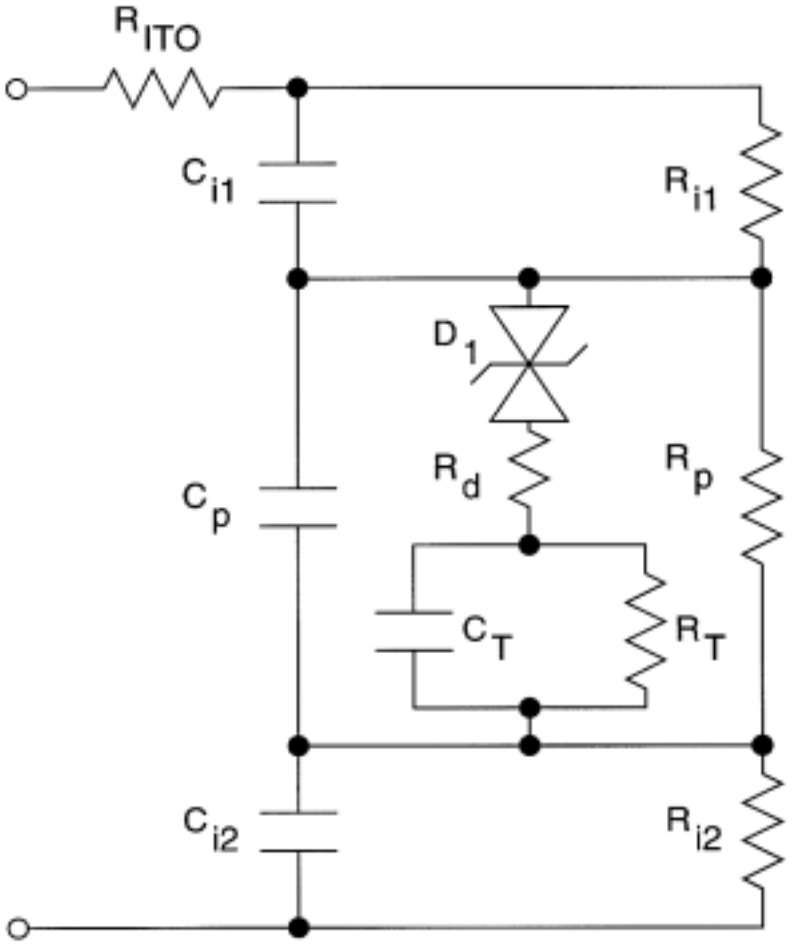

Figure 7: Douglas' equivalent circuit for an ACTFEL device. This model is identical to Davidson's model except that a parallel RC network is inserted in the back-to-back Zener diode shunt path.

switched capacitor than the inductor model.

Keir performed a device-physics-to-SPICE-model mapping of his single-sheet space charge model to obtain the two equivalent circuits shown in Figs. 11 and 12 [48, 61]. Figures 11 and 12 correspond to single-sheet space charge model equivalent circuits for an ACTFEL device in which space charge generation is assumed to occur via field-aided emission from bulk traps or via trap-to-band impact ionization, respectively. Both of these models are capable of simulating asymmetric C-V, Q-V, and Q-F_p curves typically observed for ALE ZnS:Mn ACTFEL devices.

First, consider the situation shown in Fig. 11 in which space charge generation occurs via field-aided trap emission. The phosphor is represented by two capacitors. The magnitudes of these capacitances depend on the position of the sheet, which represents the space charge centroid. The total phosphor capacitance is equal to a series combination of the two constituent phosphor capacitances, C_{p1} and C_{p2}. Each phosphor capacitor is shunted by two nonlinear, voltage-controlled current sources which account for the flow of space charge current (i.e., current due to electron

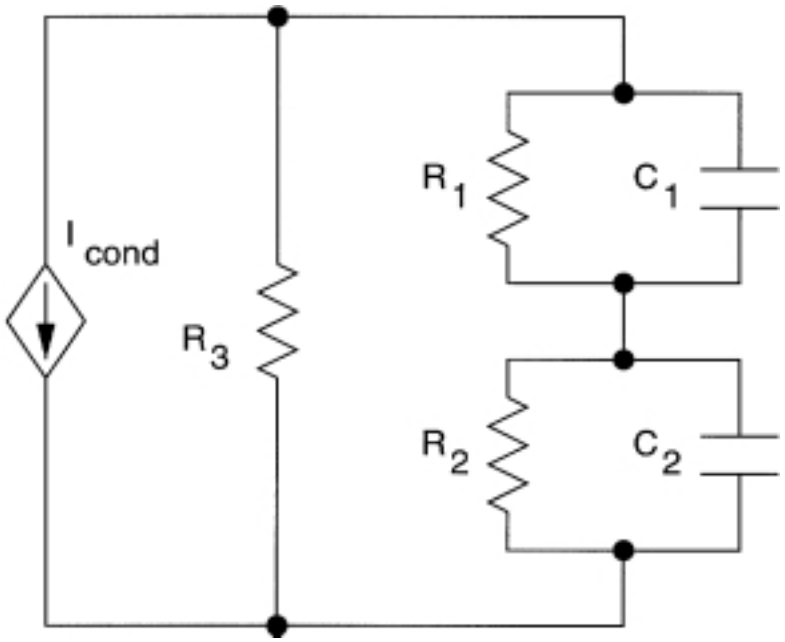

Figure 8: Douglas' optical SPICE equivalent circuit for an ACTFEL device. The current source driving the RC network arises from the instantaneous conduction current simulated using Douglas' equivalent circuit ACTFEL model. The two parallel RC branches account for two decay time constants. The instantaneous luminance of the ACTFEL device is taken as proportional to the current through the shunt resistor, R_3.

injection from the charge sheet and trapping at one of the phosphor/insulator interfaces) and leakage current (i.e., space charge annihilation current in which electrons are injected from one of the phosphor/insulator interfaces and are trapped at the charge sheet). Finally, the dual phosphor capacitance series combination is shunted by two nonlinear, voltage-controlled current sources which represent current flowing from one phosphor/insulator interface to the other. Note that the mathematical form of the current-voltage characteristics for each of the controlled sources shown in Fig. 11 is established by appropriate device physics equations.

Figure 13 illustrates the procedure used to accomplish device-physics-equations-to-SPICE-model mapping for an ACTFEL device in which space charge generation occurs via field-assisted emission from bulk traps for a positive applied voltage pulse. This procedure consists of sketching the appropriate energy band diagram, identifying the relevant charge storage and charge transfer processes, using capacitors to account for charge storage, and using controlled current sources to account for charge transport. Note that the current source directions of current flow are in an opposite direction to the direction of electron flow.

Now consider the situation shown in Fig. 12 in which space charge creation occurs via trap-to-band impact ionization. The total phosphor capacitance is equal to a series combination of the two constituent phosphor capacitances, C_{p1} and C_{p2}. Each phosphor capacitor is shunted by two branches. One shunt branch consists of a nonlinear, voltage-controlled current source which accounts for the flow of leakage current (i.e., space charge annihilation current in which electrons

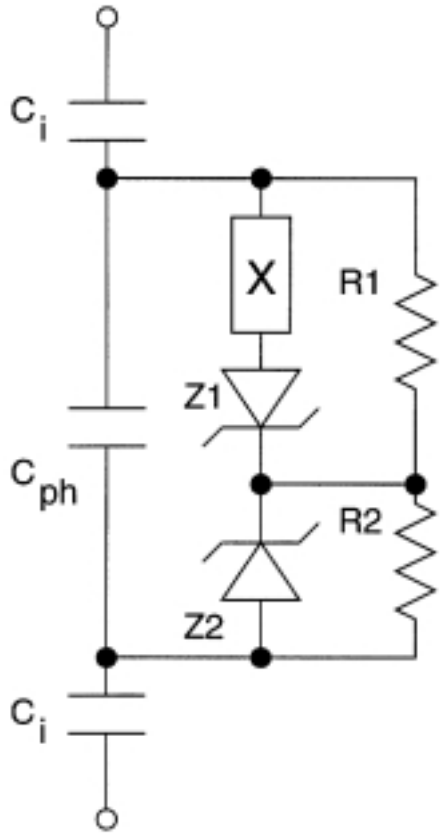

Figure 9: Åberg's equivalent circuit model for an ACTFEL device. The impedance labeled "X" in series with the Zener diode can be a (1) resistor, (2) a resistor and capacitor in series, or (3) an inductor.

are injected from one of the phosphor/insulator interfaces and are trapped at the charge sheet). The other shunt branch consists of a series combination of a nonlinear, voltage-dependent current source which represents space charge current (i.e., current due to electron injection from the charge sheet and trapping at one of the phosphor/insulator interfaces) and a nonlinear amplifier whose gain is a function of each phosphor voltage; the mathematical form of this nonlinear amplifier is established by the device physics equations describing electron multiplication by impact ionization within the phosphor. Finally, the dual phosphor capacitance series combination is shunted by two nonlinear, voltage-controlled current sources which represent current flowing from one phosphor/insulator interface to the other.

An example of the use of SPICE analysis for device physics assessment involved the interpretation of anomalous Q-V curves that were observed for several types of ACTFEL devices [62]. These Q-V curves were anomalous because conduction charge flows in these devices exclusively during the portion of the waveform in which the applied voltage is constant, at its maximum value; this kind of conduction is denoted relaxation charge since this is the portion of the applied voltage waveform in which the magnitude of the phosphor field decreases, or relaxes. SPICE simulation of this anomalous

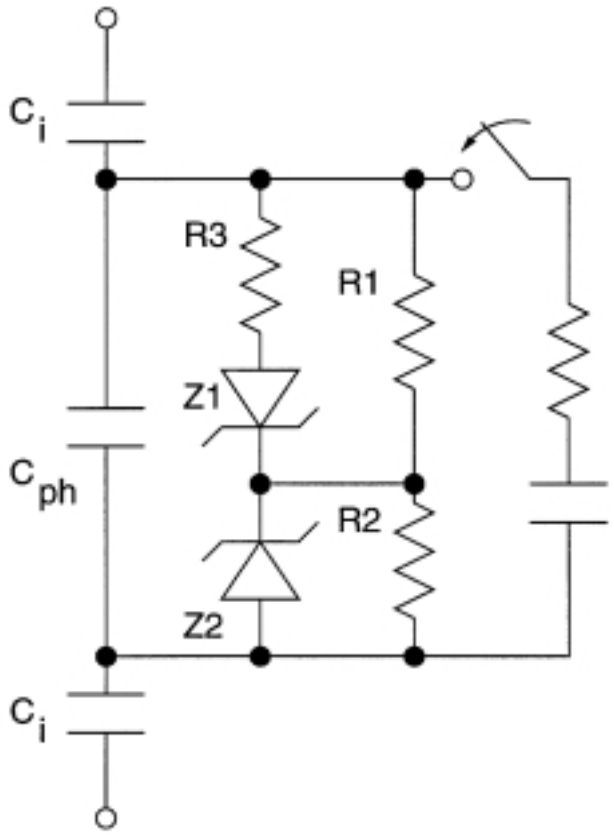

Figure 10: Åberg's switched capacitor equivalent circuit model to account for capacitance overshoot due to dynamic space charge. The switch shown is closed during the application of applied voltage pulses and is open between pulses.

relaxation charge indicated that it arises from DC leakage in one of the insulator or phosphor layers.

III. Current Actfel Modeling Activities

A. n-Sheet, State-Space Modeling

State-space analysis is a well-established approach for systematically analyzing complex dynamic systems [63, 64]. The basic ideas underlying state-space analysis are quite simple. First, the dynamic system of interest is described by a small set of time-dependent differential equations, denoted state variables **x**(t), which provide information about the internal characteristics of the system. Second, the system is presumed to be describable by an *n*th order differential equation relating the internal state variables to the external, measurable output variables. Rather than use the *n*th order differential equation to describe and analyze the system, however, the avenue of approach employed in state-space analysis is to describe the system by a set of *n* simultaneous first order differential equations.

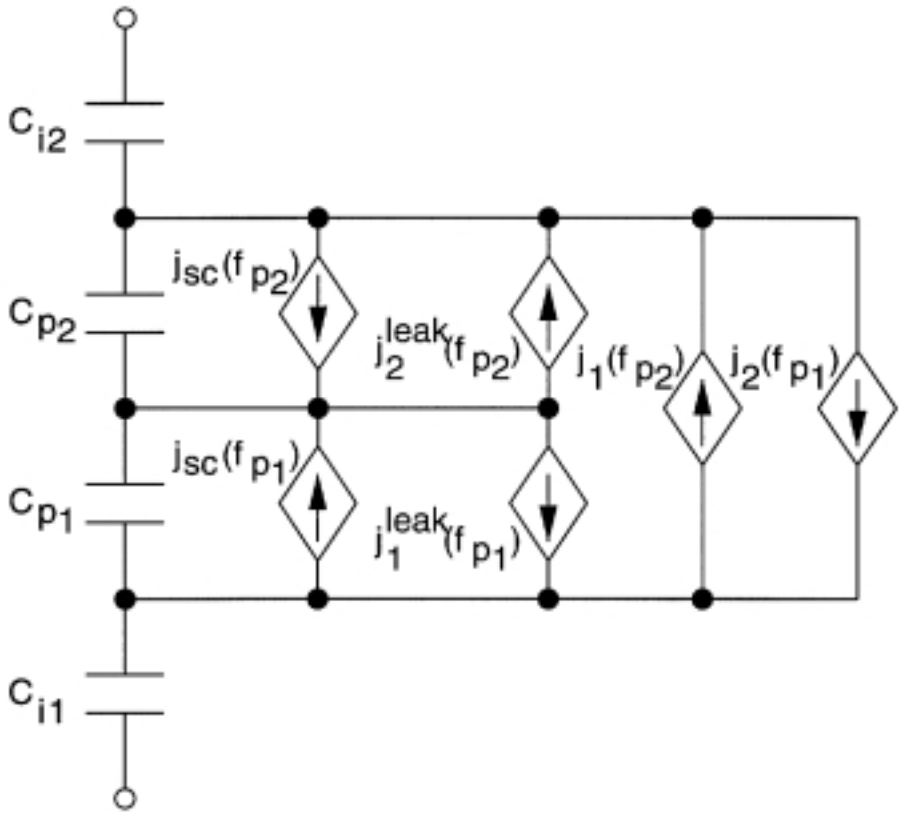

Figure 11: Keir's single-sheet space charge model equivalent circuit for an ACTFEL device in which space charge generation is assumed to occur via field-aided emission from bulk traps. Each phosphor capacitor is shunted by two nonlinear, voltage-controlled current sources which account for the flow of space charge current (i.e., current due to electron injection from the charge sheet and trapping at one of the phosphor/insulator interfaces) and leakage current (i.e., space charge annihilation current in which electrons are injected from one of the phosphor/insulator interfaces and are trapped at the charge sheet). The dual phosphor capacitance series combination is shunted by two nonlinear, voltage-controlled current sources which represent current flowing from one phosphor/insulator interface to the other.

The fundamental state-space equations describing a dynamic system may be written as:

$$\dot{\mathbf{x}}(t) = f\left[\mathbf{x}\left(t\right), \mathbf{e}\left(t\right), t\right] \tag{1}$$

$$\mathbf{y}(t) = g\left[\mathbf{x}\left(t\right), \mathbf{e}\left(t\right), t\right] \tag{2}$$

where $\mathbf{x}(t)$, the *state vector*, is just the collection of all state variables required to describe the system; $\dot{\mathbf{x}}(t)$, the *velocity vector* of the system, is the time derivative of the state variables; $\mathbf{e}(t)$ is a column vector of excitation sources (i.e., inputs); $\mathbf{y}(t)$ is a column vector representing system outputs; and t denotes time. The functions f and g shown in Eqs. (1) and (2) indicate that the state vector and the

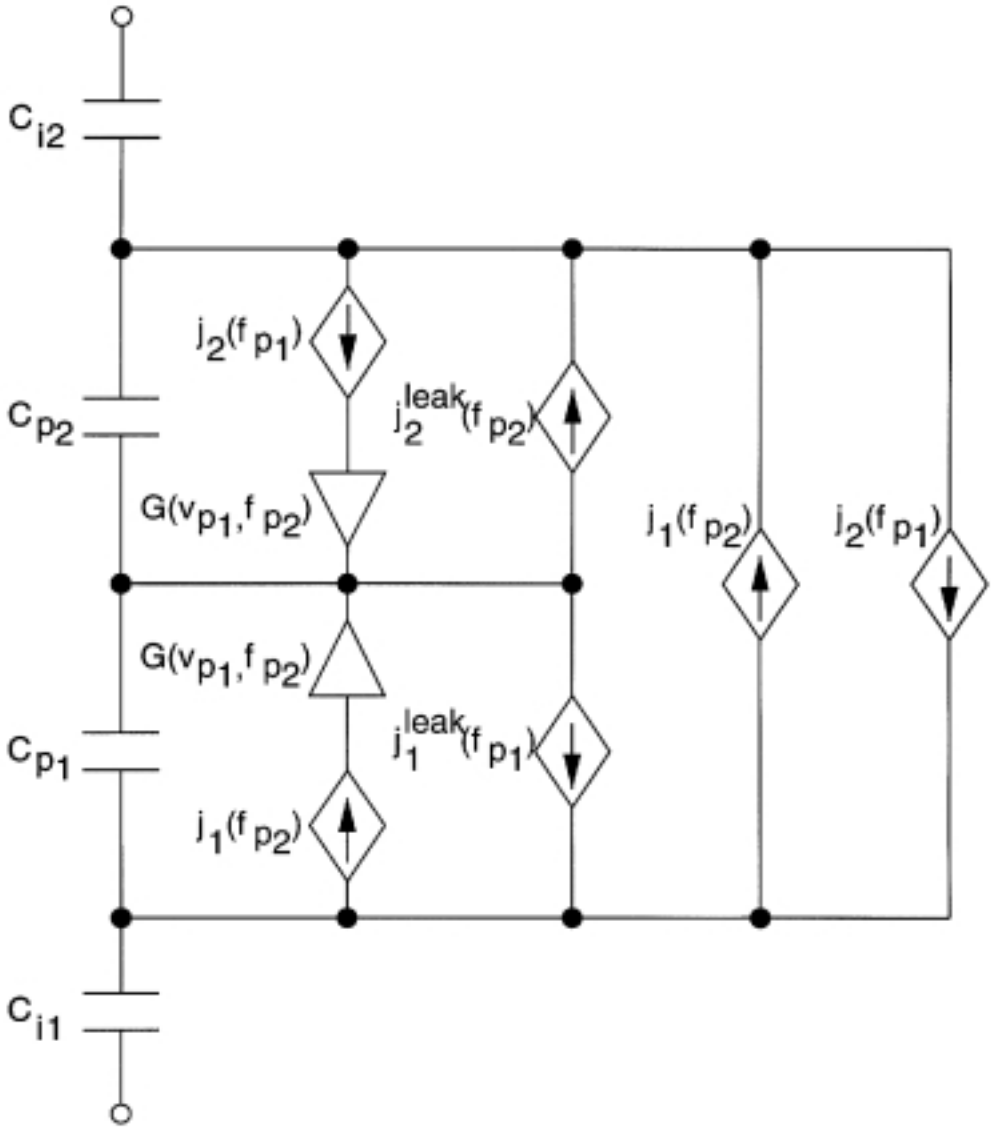

Figure 12: Keir's single-sheet space charge model equivalent circuit for an ACTFEL device in which space charge generation is assumed to occur via trap-to-band impact ionization. Each phosphor capacitor is shunted by two branches. One shunt branch consists of a nonlinear, voltage-controlled current source which accounts for the flow of leakage current (i.e., space charge annihilation current in which electrons are injected from one of the phosphor/insulator interfaces and are trapped at the charge sheet). The other shunt branch consists of a series combination of a nonlinear, voltage-dependent current source which represents space charge current (i.e., current due to electron injection from the charge sheet and trapping at one of the phosphor/insulator interfaces) and a nonlinear amplifier whose gain is a function of each phosphor voltage. The dual phosphor capacitance series combination is shunted by two nonlinear, voltage-controlled current sources which represent current flowing from one phosphor/insulator interface to the other.

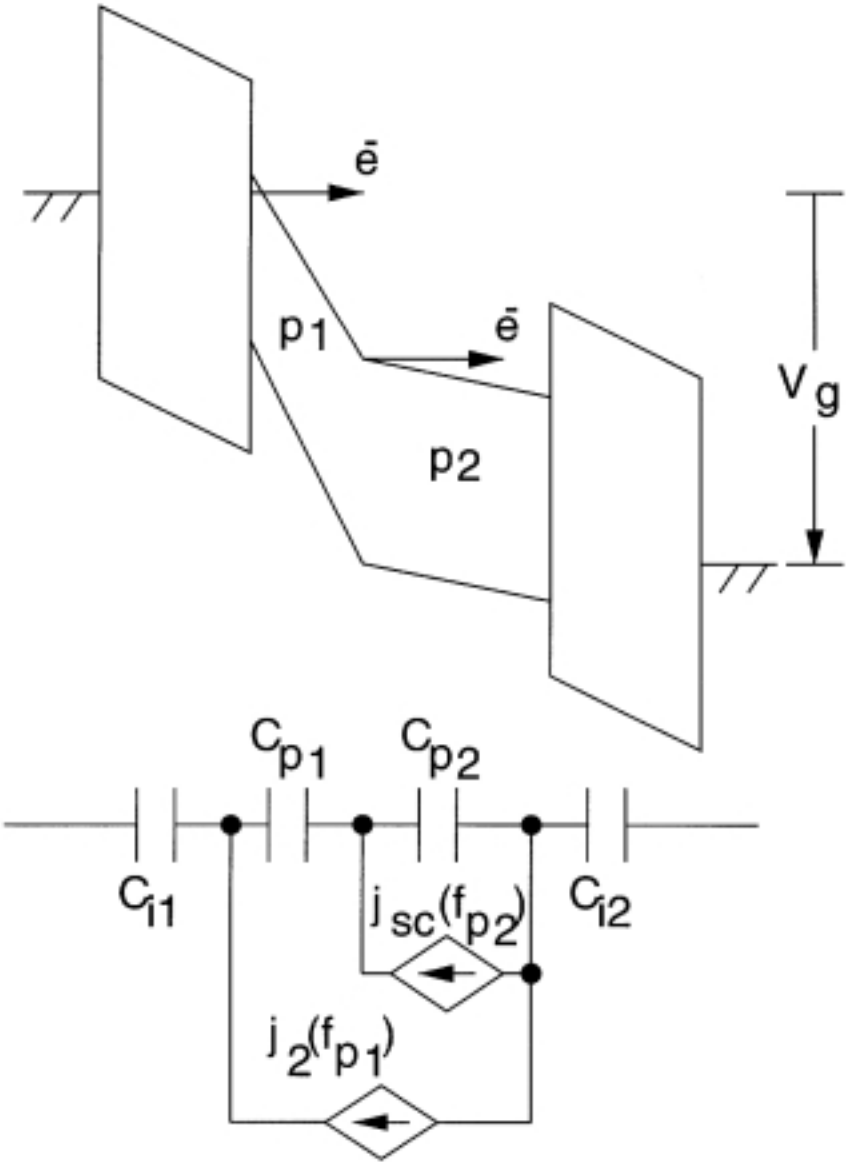

Figure 13: Energy band diagram and equivalent circuit representation of the conduction and space charge currents for an ACTFEL device in which space charge is generated via field-aided emission from bulk traps when it is subjected to a positive applied voltage pulse.

output vector are related to some algebraic function of the state and excitation vectors and perhaps time.

Besides offering an elegant way to mathematically describe a complex physical system, we have found that state-space analysis offers several additional advantages that are attractive for ACTFEL device physics modeling. First is the simplicity of the equations used for state-space analysis. Second, with such simple equations it is relatively easy to implement a state-space model on a computer. Third, there are a great number of numerical techniques used to solve a system of first order differential equations. Fourth, it is very easy to incorporate the measurement circuit elements into a state-space simulation; this is extremely difficult to do within the framework of conventional device physics [53]. Finally, the state-space methodology neatly and automatically decouples the simulation problem into two sub-problems: (1) accounting for the dynamic response of the total system (i.e., the ACTFEL device and the test circuit) and (2) device physics modeling of the internal operation of the ACTFEL device. This inherent decoupling implicit in state-space analysis allows the modeler to concentrate primarily on the device physics modeling and yet to account for the external test circuit effects in a straightforward fashion.

1. Development of ACTFEL State-Space Equations

For the development of an ACTFEL state-space model with a discretized phosphor layer, consider the equivalent circuit shown in Fig. 14. This figure shows the ACTFEL device to be simulated with the top and bottom insulators, C_{it} and C_{ib}, as ideal capacitors. The phosphor layer is discretized into N layers, C_{p1} through C_{pN}. A series resistance, R_s, which exists in an actual device measurement configuration is shown. Also shown is the voltage source used to drive the device, $v_g(t)$. The sense capacitor used in a Sawyer-Tower configuration to monitor the ACTFEL electrical performance, C_s, is shunted by the finite resistance of the oscilloscope used to measure the instantaneous voltage across C_s. In formulating the state-space equations all of the capacitances, including C_{it}, C_{ib}, C_{p1} through C_{pN}, and C_s are normalized to the ACTFEL device area, and are therefore assumed to be in units of F/cm^2. Initially, R_{scope} is neglected in the state-space formulation. Later, the oscilloscope resistance is added into the model and its effects are discussed.

Kirchhoff's Voltage Law (KVL) can be applied to solve for the current density $j(t)$ through the series resistor R_s as follows:

$$j(t) = \frac{1}{AR_s}\left(v_g(t) - v_{Cit}(t) - \sum_{n=1}^{N} v_{Cpn}(t) - v_{Cib}(t) - v_{Cs}(t)\right) \tag{3}$$

where $v_g(t)$ is the output voltage of the excitation source, $v_{Cit}(t)$ is the voltage across the top insulator, $v_{Cpn}(t)$ is the voltage across the nth phosphor element, $v_{Cib}(t)$ is the voltage across the bottom insulator, $v_{Cs}(t)$ is the voltage across the sense capacitor, and A is the device area.

An examination of the circuit of Fig. 14 shows that the current density calculated in Eq. (3) is equal to the displacement current densities of the top insulator capacitance C_{it}, and the bottom insulator capacitance C_{ib}. This current density is also equal to the displacement current density through the sense capacitance C_s ignoring, for the moment, the parasitic oscilloscope resistance, R_{scope}. Accounting for the current density in each phosphor layer is only slightly more complex. Applying Kirchhoff's Current Law (KCL) to the node between the top insulator and the top phosphor element shows that the current density calculated above is equal to the sum of the displacement current density of the first phosphor capacitance C_{p1} and the conduction current density in the first shunt

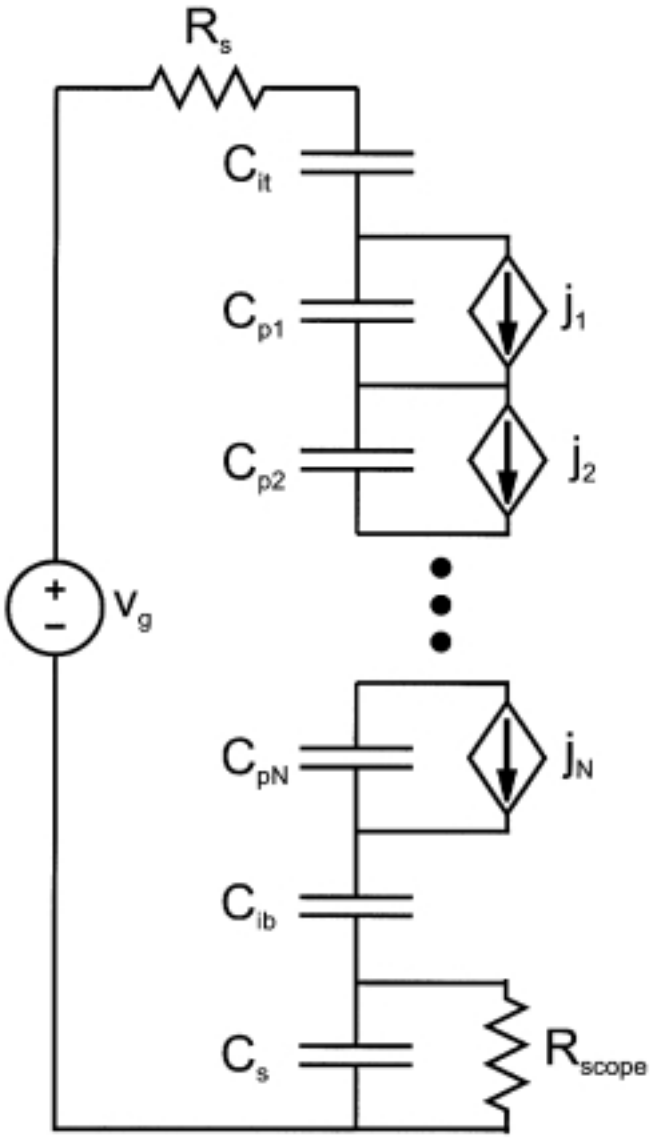

Figure 14: ACTFEL device equivalent circuit model for state-space analysis. The ACTFEL device is modeled assuming ideal top and bottom insulators, C_{it} and C_{ib}, respectively, with the phosphor layer discretized into N layers, each modeled as a capacitance, C_{pk}, shunted by a current density, j_k, with k representing the layer number. Measurement circuit elements also included in the model are the driving voltage source, v_g, the series resistance, R_s, and the sense capacitor, C_s, which is shunted by the oscilloscope resistance, R_{scope}.

element $j_1(t)$. Clearly, the relationship between the total current density $j(t)$ and the remaining phosphor elements is similar. Thus, a set of coupled differential equations is developed:

$$C_{it}\frac{dv_{Cit}(t)}{dt} = j(t) \quad (4)$$

$$C_{p1}\frac{dv_{Cp1}(t)}{dt} + j_1(t) = j(t) \quad (5)$$

$$C_{p2}\frac{dv_{Cp2}(t)}{dt} + j_2(t) = j(t) \quad (6)$$

$$\vdots$$

$$C_{pN}\frac{dv_{CpN}(t)}{dt} + j_N(t) = j(t) \quad (7)$$

$$C_{ib}\frac{dv_{Cib}(t)}{dt} = j(t) \quad (8)$$

$$C_s\frac{dv_{Cs}(t)}{dt} = j(t) \quad (9)$$

Rearranging these equations into the state-space format, where the time derivatives are isolated to the left-hand side of the equation and substituting Eq. (3) for $j(t)$ yields:

$$\frac{dv_{Cit}(t)}{dt} = \frac{1}{AR_sC_{it}}\left[v_g(t) - v_{Cit}(t) - \sum_{n=1}^{N} v_{Cpn}(t) - v_{Cib}(t) - v_{Cs}(t)\right] \quad (10)$$

$$\frac{dv_{Cp1}(t)}{dt} = \frac{1}{AR_sC_{p1}}\left[v_g(t) - v_{Cit}(t) - \sum_{n=1}^{N} v_{Cpn}(t) - v_{Cib}(t) - v_{Cs}(t)\right] - \frac{j_1(t)}{C_{p1}} \quad (11)$$

$$\frac{dv_{Cp2}(t)}{dt} = \frac{1}{AR_sC_{p2}}\left[v_g(t) - v_{Cit}(t) - \sum_{n=1}^{N} v_{Cpn}(t) - v_{Cib}(t) - v_{Cs}(t)\right] - \frac{j_2(t)}{C_{p2}} \quad (12)$$

$$\vdots$$

$$\frac{dv_{CpN}(t)}{dt} = \frac{1}{AR_sC_{pN}}\left[v_g(t) - v_{Cit}(t) - \sum_{n=1}^{N} v_{Cpn}(t) - v_{Cib}(t) - v_{Cs}(t)\right] - \frac{j_N(t)}{C_{pN}} \quad (13)$$

$$\frac{dv_{Cib}(t)}{dt} = \frac{1}{AR_sC_{ib}}\left[v_g(t) - v_{Cit}(t) - \sum_{n=1}^{N} v_{Cpn}(t) - v_{Cib}(t) - v_{Cs}(t)\right] \quad (14)$$

$$\frac{dv_{Cs}(t)}{dt} = \frac{1}{AR_sC_s}\left[v_g(t) - v_{Cit}(t) - \sum_{n=1}^{N} v_{Cpn}(t) - v_{Cib}(t) - v_{Cs}(t)\right] \quad (15)$$

Equations 11 to 16 are a series of coupled differential equations (i.e., the state-space equations), which can be solved to obtain the dynamic response of the system. Stated in matrix form, the

state-space equations are:

$$\begin{bmatrix} \dot{v}_{it}(t) \\ \dot{v}_{p1}(t) \\ \dot{v}_{p2}(t) \\ \vdots \\ \dot{v}_{pN}(t) \\ \dot{v}_{ib}(t) \\ \dot{v}_{Cs}(t) \end{bmatrix}$$

$$= \frac{1}{AR_s} \begin{bmatrix} -\frac{1}{C_{it}} & -\frac{1}{C_{it}} & -\frac{1}{C_{it}} & \cdots & -\frac{1}{C_{it}} & -\frac{1}{C_{it}} & -\frac{1}{C_{it}} \\ -\frac{1}{C_{p1}} & -\frac{1}{C_{p1}} & -\frac{1}{C_{p1}} & \cdots & -\frac{1}{C_{p1}} & -\frac{1}{C_{p1}} & -\frac{1}{C_{p1}} \\ -\frac{1}{C_{p2}} & -\frac{1}{C_{p2}} & -\frac{1}{C_{p2}} & \cdots & -\frac{1}{C_{p2}} & -\frac{1}{C_{p2}} & -\frac{1}{C_{p2}} \\ \vdots & \vdots & \vdots & & \vdots & \vdots & \vdots \\ -\frac{1}{C_{pN}} & -\frac{1}{C_{pN}} & -\frac{1}{C_{pN}} & \cdots & -\frac{1}{C_{pN}} & -\frac{1}{C_{pN}} & -\frac{1}{C_{pN}} \\ -\frac{1}{C_{ib}} & -\frac{1}{C_{ib}} & -\frac{1}{C_{ib}} & \cdots & -\frac{1}{C_{ib}} & -\frac{1}{C_{ib}} & -\frac{1}{C_{ib}} \\ -\frac{1}{C_s} & -\frac{1}{C_s} & -\frac{1}{C_s} & \cdots & -\frac{1}{C_s} & -\frac{1}{C_s} & -\frac{1}{C_s} \end{bmatrix} \begin{bmatrix} v_{it}(t) \\ v_{p1}(t) \\ v_{p2}(t) \\ \vdots \\ v_{pN}(t) \\ v_{ib}(t) \\ v_{Cs}(t) \end{bmatrix} + \cdots$$

$$+ \frac{1}{AR_s} \begin{bmatrix} \frac{1}{C_{it}} \\ \frac{1}{C_{p1}} \\ \frac{1}{C_{p2}} \\ \vdots \\ \frac{1}{C_{pN}} \\ \frac{1}{C_{ib}} \\ \frac{1}{C_s} \end{bmatrix} v_g(t) - \begin{bmatrix} 0 & 0 & \cdots & 0 \\ \frac{1}{C_{p1}} & 0 & \cdots & 0 \\ 0 & \frac{1}{C_{p2}} & \cdots & 0 \\ \vdots & \vdots & & \vdots \\ 0 & 0 & \cdots & \frac{1}{C_{pN}} \\ 0 & 0 & \cdots & 0 \\ 0 & 0 & \cdots & 0 \end{bmatrix} \begin{bmatrix} j_1(t) \\ j_2(t) \\ \vdots \\ j_N(t) \end{bmatrix} \tag{16}$$

Alternatively, the state-space equations may be expressed in vector form as:

$$\dot{\mathbf{v}}(t) = \mathbf{A}\mathbf{v}(t) + \mathbf{B}v_g(t) - \mathbf{C}\mathbf{j}(t) \tag{17}$$

Note that in Eq. (17) the linear response of the ACTFEL equivalent circuit is contained in the $\mathbf{A}\mathbf{v}(t) + \mathbf{B}v_g(t)$ term and the nonlinearities are encapsulated in the $\mathbf{C}\mathbf{j}(t)$ term. Additionally, all of the device physics of the phosphor layer are implemented in the analytical formulation of $\mathbf{j}(t)$. The analytical formulation of these current densities is presented later in this review. Once mathematical expressions for these current densities have been specified, the state-space differential equations are solved numerically using a fifth-order Runge-Kutta algorithm.

2. Interface State Emission Mechanisms

In implementing the device physics of the phosphor layer it is appropriate to start with the injection of electrons from the phosphor-insulator interface into the phosphor layer. The possible emission mechanisms for a trapped electron are (1) thermionic emission, (2) pure tunneling, and (3) phonon-assisted tunneling. These emission mechanisms are illustrated in Fig. 15. Thermionic emission occurs when a trapped carrier gains enough energy from phonons to surmount the barrier and be injected into the conduction band. Pure tunneling occurs at high fields when the barrier is thin

enough that trapped carriers can tunnel directly into the conduction band from the trap. Finally, phonon-assisted tunneling is a hybrid process where a carrier gains some energy from phonons and then undergoes a tunneling event into the conduction band from this higher energy level. The total trap emission rate is given by the sum of these three mechanisms

$$e_n = e_n^{thermal} + e_n^{PT} + e_n^{PAT}. \tag{18}$$

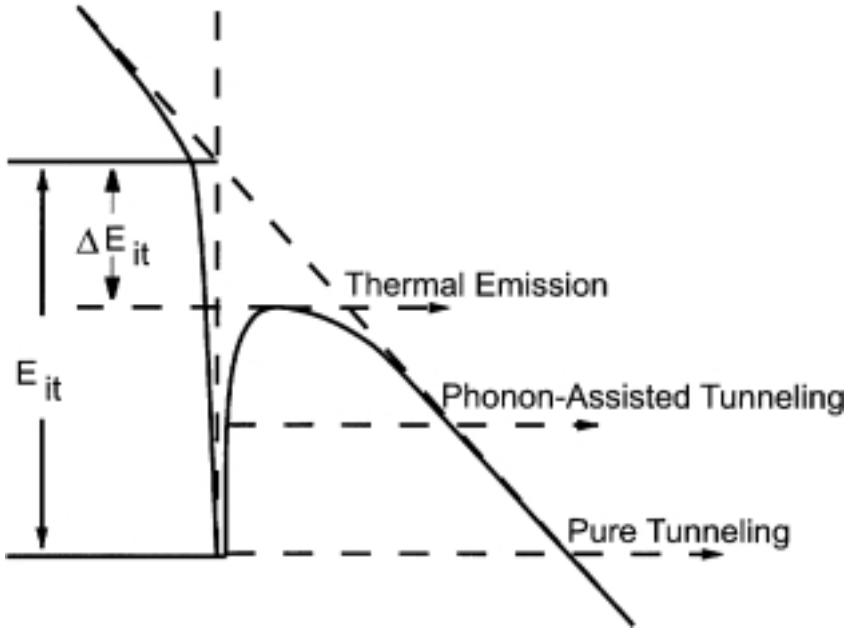

Figure 15: Emission mechanisms for an electron at a trap. Thermal emission occurs when an electron gains sufficient energy from phonons to surmount the barrier, pure tunneling is the direct injection of an electron from the trap into the conduction band, and phonon-assisted tunneling occurs when an electron gains some energy from phonons and then undergoes a tunneling event.

Fortunately, analytical expressions exist for all three of these mechanisms [18, 65, 66]. The expression for the thermal emission rate from a discrete state is given by

$$e_n^{thermal} = \sigma v_{th} N_c exp\left(-\frac{E_{it} - \Delta E_{it}}{kT}\right) \tag{19}$$

where σ is the capture cross-section, v_{th} is the thermal velocity, N_c is the conduction band density of states, k is Boltzmann's constant, T is the absolute temperature, and E_{it} is the interface trap depth. ΔE_{it} is the coulombic barrier lowering, given by

$$\Delta E_{it} = q\sqrt{\frac{qf_p}{\pi\epsilon_p}} \tag{20}$$

where f_p is the electric field (with the appropriate sign for electron injection) in the phosphor region at the interface of interest. The emission rate due to pure tunneling, e_n^{PT}, is given by

$$e_n^{PT} = \frac{qf_p}{4\left(2m^* E_{it}\right)^{\frac{1}{2}}} exp\left[\left(-\frac{4}{3}\frac{(2m^*)^{\frac{1}{2}}\, E_{it}^{\frac{3}{2}}}{q\hbar f_p}\right)\left(1-\left(\frac{\Delta E_{it}}{E_{it}}\right)^{\frac{5}{3}}\right)\right] \tag{21}$$

where m^* is the electron effective mass. Finally, the emission rate due to phonon-assisted tunneling e_n^{PAT} is given by

$$e_n^{PAT} = e_n^{thermal} \int_{\frac{\Delta E_{it}}{kT}}^{\frac{E_{it}}{kT}} exp\left[z - z^{\frac{3}{2}}\left(\frac{4}{3}\frac{(2m^*)^{\frac{1}{2}}\,(kT)^{\frac{3}{2}}}{q\hbar f_p}\right)\left(1-\left(\frac{\Delta E_{it}}{zkT}\right)^{\frac{5}{3}}\right)\right] dz. \tag{22}$$

Equations 19, 21, and 22 can be inserted into Eq. (18) to calculate the total emission rate. The electron current density leaving an interface, j_n, is then calculated from

$$j_n = n_{it} e_n \tag{23}$$

where n_{it} is the density of filled traps at the interface, which can be calculated using the electrostatic boundary condition of the phosphor-insulator interface.

For interfaces modeled as discrete traps with a trap depth of about 1.5 eV, pure tunneling is the dominant emission mechanism at high fields; at low fields the emission rate is negligible for a trap of this depth. Thus, many researchers utilize only pure tunneling as the interface emission mechanism [16, 18, 19, 36, 42, 43]. Some researchers use all three mechanisms [48, 54].

3. Charge Multiplication

Once injected from the interface into the phosphor layer, an electron drifts subject to the phosphor electric field. It may be possible for the electron to gain sufficient energy such that a collision with the lattice results in a band-to-band impact ionization event, thus generating a hole in the valence band and an additional electron in the conduction band. The average number of impact ionization events for an electron per unit length traveled is defined as the ionization function, α_n. Bringuier [19] gives this function as

$$\alpha_n = \left(\frac{qf}{E_i}\right) exp\left[-\left(\frac{F_0}{f}\right)^n\right] n = 1, 2, \tag{24}$$

with E_i the effective ionization energy and F_0 the characteristic field for impact ionization. The multiplication factor, m, for electrons traveling a length d across the phosphor is given by

$$m = exp\left[d\alpha_n\right]. \tag{25}$$

Consider two sections of the discretized phosphor layer, as shown in the energy band diagram of Fig. 16. The electron and hole current densities are displayed along with other physical processes to be discussed later. Using this diagram as a guide, the implementation of electron emission and band-to-band impact ionization is as follows. For the top phosphor-insulator interface, with $k = 1$, the two current components are calculated as follows:

$$j_{n,1} = n_{it} e_n \tag{26}$$

$$j_{p,1} = (m_1 - 1)\, j_{n,1} + j_{p,2}. \tag{27}$$

Note that it is necessary to add the hole current density which flows from the next phosphor layer, $j_{p,2}$.

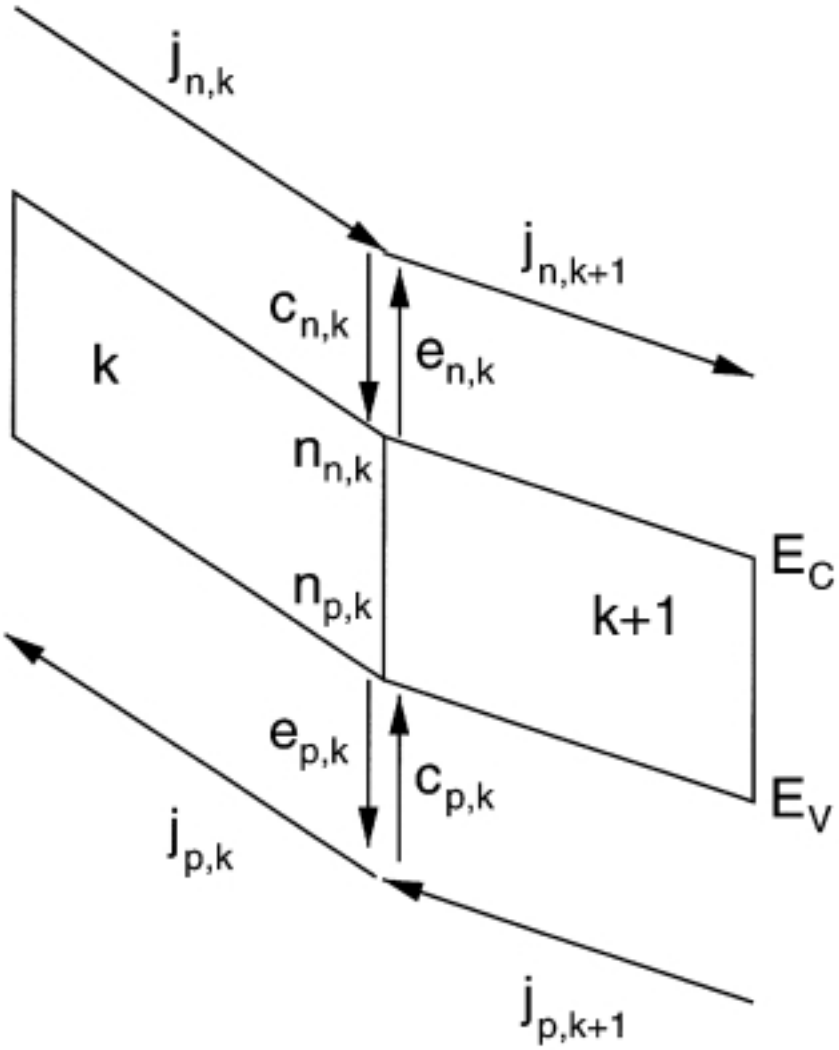

Figure 16: A general interface between phosphor layers. $j_{n,k}$ and $j_{n,k+1}$ are electron current densities with $c_{n,k}$ representing a capture factor for electrons at the sheet and $e_{n,k}$ the emission rate for electrons trapped at the sheet. Similar designations are shown for holes.

For the next phosphor element, the currents are calculated as follows:

$$j_{n,2} = m_1 j_{n,1} \tag{28}$$

$$j_{p,2} = (m_2 - 1)\, j_{n,2} + j_{p,3}. \tag{29}$$

In general:

$$j_{n,k} = m_{k-1} j_{n,k-1} \tag{30}$$

and

$$j_{p,k} = (m_k - 1)\, j_{n,k} + j_{p,k+1} \tag{31}$$

except for the case where $k = N$ (the phosphor element at the anodic interface), where $j_{p,N}$ is given by:

$$j_{p,N} = (m_N - 1)\, j_{n,N}. \tag{32}$$

4. Space Charge Generation

The generation of positive space charge in the phosphor layer is assumed to result from one of three possible processes: (1) band-to-band impact ionization and subsequent hole trapping, (2) field ionization of electron traps, and (3) trap-to-band impact ionization. With the inclusion of band-to-band impact ionization the first of these mechanisms, involving hole trapping, can be implemented. This is accomplished by allowing the band-to-band impact ionized holes to be trapped as sheet charges at the phosphor discretization boundaries. The first step in this implementation is to calculate the sheet density of hole traps, N_{pt}. This is done by multiplying the volume density of hole traps, N_p, by the total phosphor layer thickness, d_p, and dividing by the number of sheets,

$$N_{pt} = \frac{N_p d_p}{N - 1}. \tag{33}$$

It is assumed that the percentage of holes traversing a sheet that are trapped is a function of the sheet density of hole traps, the number of hole traps which have trapped holes, n_p, and the capture cross-section of these traps, σ_p. n_p can be calculated using the electro-static boundary condition. A capture factor for holes, c_p, can be calculated from

$$c_p = \sigma_p \left(N_{pt} - n_p\right) \tag{34}$$

with the value limited to $0 \leq c_p \leq 1.0$. Thus, with the inclusion of hole trapping and re-emission, the equation for calculating the hole current for an arbitrary phosphor layer [Eq. (31)] becomes

$$j_{p,k} = (m_k - 1)\, j_{n,k} + \left(1 - c_{p,k}\right) j_{p,k+1} + e_p n_{p,k} \tag{35}$$

where $c_{p,k}$ is the hole capture factor for the kth sheet, $n_{p,k}$ is the density of trapped holes calculated for the kth sheet, and $e_{p,k}$ is the hole emission rate for the kth sheet, calculated using the same emission mechanisms considered in Section 2.. With the implementation of hole capture and emission, space charge effects (static and dynamic) can be simulated.

The second space charge creation mechanism that can be implemented involves field ionization of electron traps in the phosphor layer. Electron emission from these traps can be accomplished via the three processes shown in Fig. 15. Note that dynamic space charge can be simulated via this field ionization mechanism only if electron capture at ionized electron traps is also implemented to account for space charge annihilation. An electron trap capture factor can be calculated considering

N_{nt}, the density of electron traps at the sheet, n_n, the density of filled electron traps, and σ_n, the electron capture cross-section,

$$c_n = \sigma_n \left(N_{nt} - n_n\right) \tag{36}$$

with the value limited to $0 \leq c_n \leq 1.0$. Thus, when electron trapping and re-emission are included for the field emission space charge creation mechanism, the general electron current density expression for an arbitrary phosphor sheet becomes

$$j_{n,k} = m_{k-1}\left(1 - c_{n,k-1}\right) j_{n,k-1} + e_{n,k-1} n_{n,k-1}. \tag{37}$$

The third space charge creation mechanism that can be implemented involves impact ionization of deep traps. Also denoted trap-to-band impact ionization, this event occurs when a conduction band electron transfers sufficient energy to a trapped electron to promote it to the conduction band. Implementation of trap-to-band impact ionization is very similar to band-to-band impact ionization with the exception that no valence band hole is created and the positive charge is localized at the ionized deep trap. Similar to the case of positive space charge creation by field emission, for trap-to-band impact ionization to result in dynamic space charge, the ionized traps must be allowed to capture conduction band electrons; this can be modeled in the same manner as for field ionization using Eq. (36). Thus, when electron trapping and re-emission are included for the trap-to-band impact ionization space charge creation mechanism, the electron current density expression for an arbitrary sheet becomes

$$j_{n,k} = m_{k-1}\left(1 - c_{n,k-1}\right) j_{n,k-1} + m_k^{tbii} j_{n,k-1} \tag{38}$$

where m_k^{tbii} is the trap-to-band impact ionization multiplier for the kth sheet.

5. ACTFEL State-Space Simulation Results

The utility of state-space simulation is illustrated by four examples. The first is the inclusion of measurement circuit parasitics and their effects, from which it is shown that modifying the state-space model to account for parasitics is almost trivial. The second example shows the effect of space charge on a C-V curve; from this simulation, dynamic and static space charge can be unambiguously defined. The third example is simulation of EL thermal quenching in which there is an increase in the ACTFEL device threshold voltage with increasing temperature. Finally, a simulation is run to show the differences in ACTFEL device internal characteristics (i.e., the distribution of space charge in the phosphor layer), which result from the formation of dynamic space charge originating from band-to-band impact ionization and subsequent hole trapping, or from dynamic space charge originating from trap-to-band impact ionization. Table 1 lists typical simulation parameters; deviations from these parameters are noted where relevant.

The addition of measurement circuitry parasitics is easily accomplished with state-space analysis. For example, consider the oscilloscope resistance R_{scope} shown in Fig. 14. In order to account for R_{scope} in the state-space equations, all that is necessary is to alter Eq. (9) as follows:

$$C_s \frac{dv_{Cs}(t)}{dt} + \frac{1}{A}\frac{v_{Cs}}{R_{scope}} = j(t). \tag{39}$$

Table 1: Nominal ACTFEL state-space device simulation parameters.

Simulation Parameter	Value	Simulation Parameter	Value
Phosphor Thickness	650 nm	Interface Trap Depth	1.5 eV
Phosphor Dielectric Constant	8.3	Neutral Interface Trap Density	5×10^{13} cm^{-2}
Phosphor Discretization	10 layers	Hole Trap Density	1×10^{16} cm^{-3}
Top Insulator Thickness	180 nm	Hole Trap Depth	1.2 eV
Top Insulator Dielectric Constant	6.5	Hole Trap Capture Cross Section	1×10^{-12} cm^2
Bottom Insulator Thickness	110 nm	Series Resistance	500 Ω
Bottom Insulator Dielectric Constant	6.5	Sense Capacitance	103.9 nF
Rise Time	5 μs	BBII Characteristic Field *	1.9 MV/cm
Pulse Width	30 μs	BBII Ionization Energy *	5.4 eV
Fall Time	5 μs	Temperature	300 K
Frequency	1000 Hz	Cycles Simulated	5

*BBII = Band-to-Band Impact Ionization

The resulting altered equation in the state-space format is

$$\frac{dv_{Cs}(t)}{dt} = \frac{1}{AR_sC_s}\left[v_g(t) - v_{Cit}(t) - \sum_{n=1}^{N} v_{Cpn}(t) - v_{Cib}(t) - v_{Cs}(t)\right] - \frac{v_{Cs}}{AR_{scope}C_s}. \quad (40)$$

Note that the inclusion of R_{scope} results in the modification of the last element in the bottom row of the **A** matrix ($m \times m$) of the vector form of the state-space equations (Eq. (17)) which becomes:

$$A_{m,m} = \left(-\frac{1}{AR_sC_s} - \frac{R_s}{AC_sR_{scope}}\right). \quad (41)$$

The most important effect of the inclusion of the finite oscilloscope resistance in the simulation is the loss of any DC voltage component which may have existed on the sense capacitor. One electrical characteristic for which this is an important characteristic is offset. Electrical offset is the shifting of a Q-V curve along the vertical axis. Offset has been attributed to asymmetries in interface state energy depths which would lead to more charge transferred in one direction for the first few pulses of device operation than in the steady-state when equal amounts of charge are transferred in each direction [18, 50]. However, while asymmetries in interface state energy depths will cause an offset for a very short period of time, the DC voltage information will gradually "leak" off the sense capacitor and result in Q-V curves that show no offset effect when steady-state operation is attained. The decay rate of the DC voltage information stored on the sense capacitor depends upon the $R_{scope}C_s$ time constant.

Figure 17 shows the results of a state-space simulation of an ACTFEL device with a top interface trap depth of 0.8 eV and a bottom interface trap depth of 1.5 eV with the oscilloscope resistance set to 10 MΩ. Three Q-V curves are shown, one for the 5th cycle of a device starting from flat-band, one for the 1000th cycle, and one for the 5000th cycle. Note that the 5-cycle curve is shifted downward along the vertical axis which is indicative of electrical offset. This downward shift results from the initial asymmetric transfer of electrons from the top interface to the bottom interface. If this asymmetric transfer of electrons occurs from the bottom interface to the top interface, the polarity of

the offset is reversed. Also note that the 5000th cycle curve shows little if any offset, since after 5000 cycles the DC voltage component is almost completely lost. The use of a high input impedance buffer amplifier between the sense capacitor and oscilloscope is one way to maintain the DC component on the sense capacitor [67, 68].

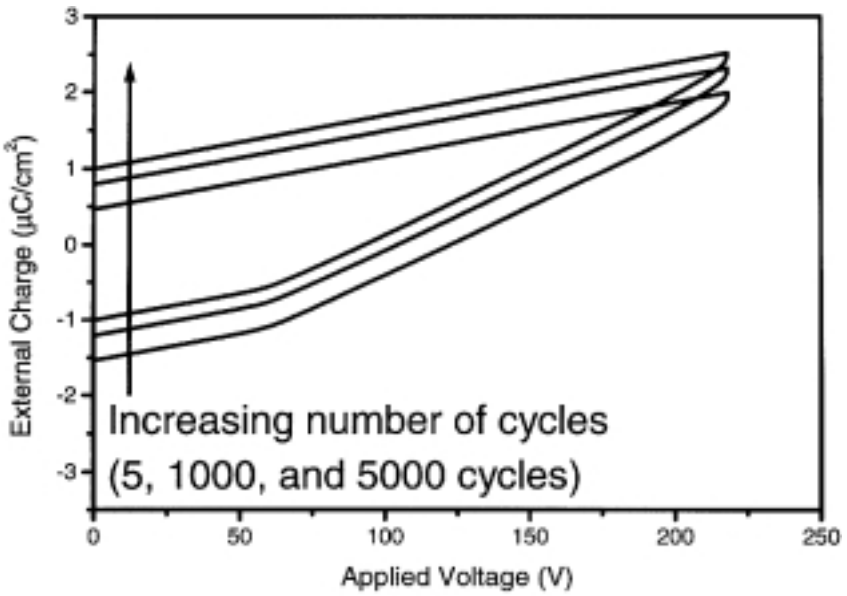

Figure 17: Simulated Q-V curves using asymmetric interface trap depths to create an electrical offset. Curves are simulated for 5, 1000, and 5000 cycles. Note that with an increasing number of cycles simulated, the magnitude of the offset decreases. This is due to the decay of the DC voltage component of the sense capacitor caused by the finite oscilloscope resistance, R_{scope}.

Another example of state-space simulation is the effect of the series resistance, R_s, on the electrical characteristics. Figure 18 shows C-V curves generated from four simulations where the device parameters are constant with the exception of the series resistance. Space charge creation is modeled assuming band-to-band impact ionization and subsequent hole trapping with a hole trap density of 5×10^{17} cm^{-3} and a hole trap depth of 0.7 eV. It is evident from Fig. 18 that the C-V overshoot is significantly larger for the case of the 500 Ω and 1000 Ω series resistances. Note that it has proven difficult to implement series resistance effects in device physics simulations that are not based on the state-space approach [53].

State-space analysis can also clearly and unambiguously elucidate the effects of dynamic and static space charge in ACTFEL device electrical characteristics. In order to accomplish this, a simulation is performed in which band-to-band impact ionization and subsequent hole trapping is assumed to be the space charge creation mechanism, with a hole trap density of 5×10^{17} cm^{-3}. The hole trap depth is set sufficiently shallow (0.7 eV) to allow for appreciable emission of holes from these traps to the valence band, as space charge annihilation is a prerequisite for dynamic space charge. Figure 19 shows a C-V curve and a plot of the total space charge density. Note that overshoot in the C-V curve occurs concomitantly with a steep rise in space charge density. Also note that the space charge density remains relatively constant at the lower voltages; this constitutes the

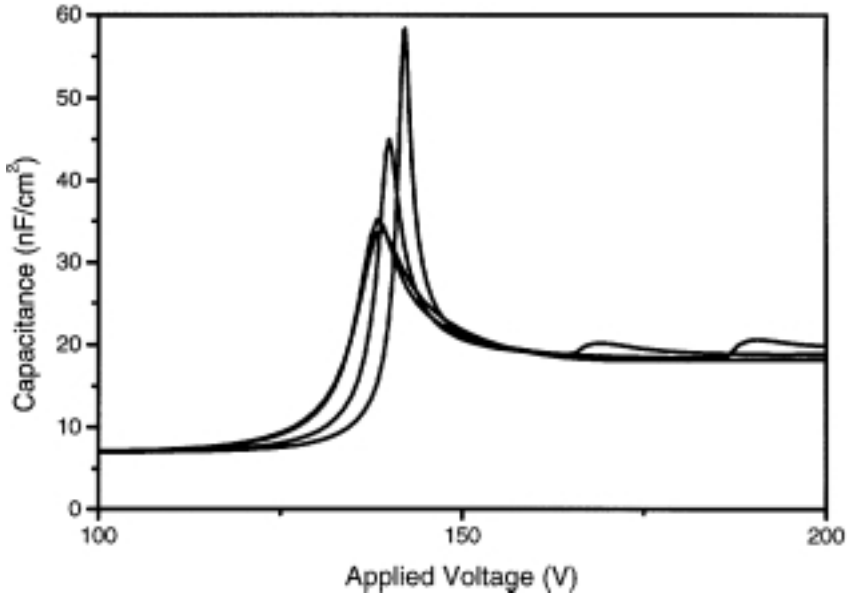

Figure 18: Simulated C-V curves showing the effects of the series resistance on overshoot. With all other parameters held constant, simulations are performed for series resistances of 50, 100, 500, and 1000 Ω. Note the increase in overshoot with increasing series resistance.

static component of the space charge. Accordingly, the dynamic space charge portion is identified as the difference between the maximum and minimum amount of space charge, as shown in Fig. 19. The decrease in the total space charge density just prior to the turn-on voltage arises from the field emission of holes from phosphor layer hole traps. Finally, the "bump" in the C-V curve seen at about 180 V is an RC effect involving the series resistance.

One of the more recent issues involving ACTFEL devices is a phenomenon known as EL thermal quenching [69]. EL thermal quenching refers to an increase in the threshold voltage of an ACTFEL device corresponding to an increase in the temperature. In addition to an increased threshold voltage, there is also a decrease in the amount of overshoot in a transferred charge capacitance curve. While EL thermal quenching does not occur for all ACTFEL devices, it has been shown to occur in some of the more recently developed phosphors, including SrS:Cu. Using state-space simulation, it can be shown that one physical process that may cause EL thermal quenching is the prethreshold trapping and emission of holes. It has been shown that for ZnS:Mn, a significant amount of space charge exists in the phosphor layer below threshold [70]. This prethreshold formation of phosphor layer space charge could also occur for other phosphors. If this prethreshold space charge concentration is reduced by a thermally activated process, one would expect to see an increase in the threshold voltage.

Figure 20 shows the results of two transferred charge simulations in which band-to-band impact ionization and subsequent hole trapping is the space charge creation mechanism. Transferred charge curves are obtained by plotting the maximum value of the Q-V curve in steady-state operation with the maximum voltage applied across the ACTFEL device. For this plot, a hole trap density of 7×10^{16} cm^{-3} is assumed with a hole trap depth of 0.7 eV. Note that for the higher temperature

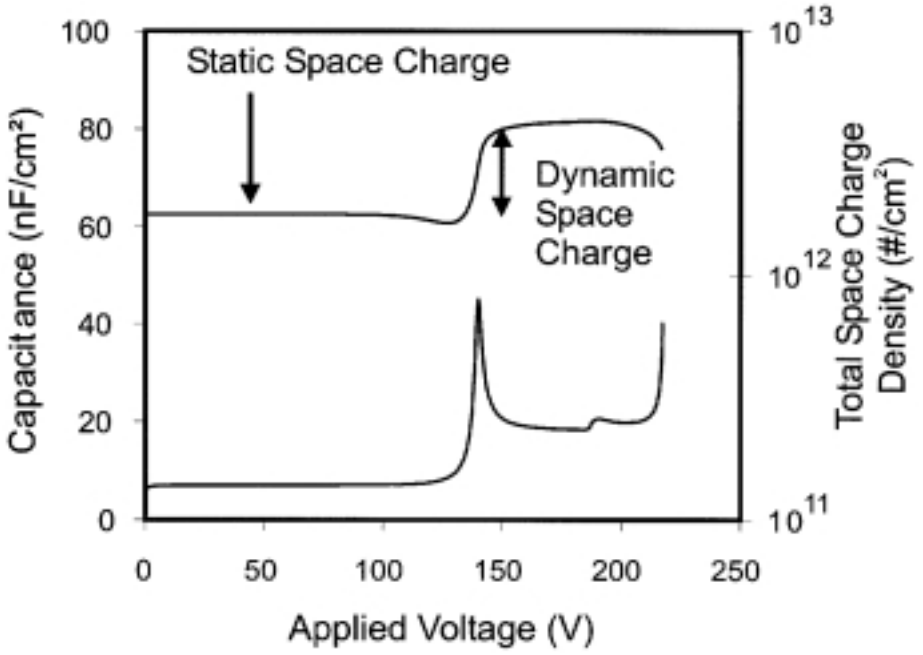

Figure 19: Simulated C-V curve and total space charge density vs. applied voltage curve for an ACTFEL device with dynamic space charge. Note the capacitance overshoot occurs concomitantly with the increase in space charge. Also note that static space charge can be defined as the space charge density prior to the positive pulse and dynamic space charge can be defined as the difference between the minimum and maximum amounts of space charge. The small dip in total space charge density just prior to turn-on is a result of space charge annihilation due to hole emission in the phosphor layer.

simulation, the threshold voltage is increased and the amount of transferred charge capacitance overshoot is decreased. Figure 21 shows the same transferred charge curve along with the steady-state amount of space charge in the device calculated just prior to the positive voltage pulse. Note that for the higher temperature the amount of space charge is reduced, resulting in a higher threshold voltage. Thus, EL thermal quenching could be caused by the thermally activated annihilation of positive space charge due to the emission of holes trapped in the phosphor layer.

With the apparent association of EL thermal quenching and prethreshold hole emission, it is interesting to consider methods of reducing this effect. Theoretically, the elimination of all phosphor layer hole traps would eliminate this problem, although in practice this is not realistic. Another method would be the elimination of the emission of the trapped holes. This could be accomplished by pushing the hole traps to a deeper energy. Figure 22 shows simulation results for an ACTFEL device in which all parameters are identical to the device simulated for Fig. 20 with the exception of the hole trap depth, which has been increased to 1.0 eV. Note that the change in threshold voltage has been substantially reduced. Simulations for hole traps deeper than 1.0 eV produce transferred charge curves which have essentially no threshold voltage difference.

State-space simulation can also provide information regarding ACTFEL device operation that

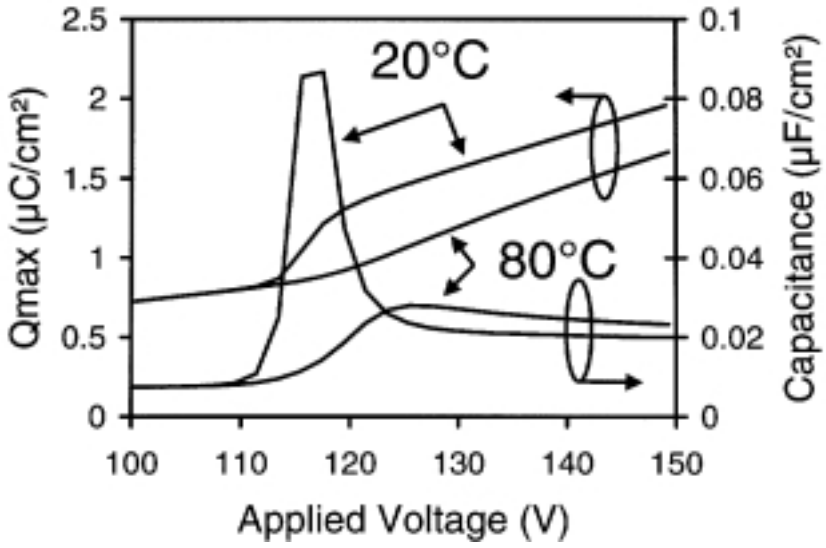

Figure 20: Simulated transferred charge and transferred charge capacitance curves for temperatures of 20° and 80°C. Note the increase in threshold voltage, which is termed EL thermal quenching. A hole trap depth of 0.7 eV and a hole trap density of 7×10^{16} cm^{-3} is used for this simulation.

is not available through the characterization of actual devices. Information regarding the density of space charge at each point in the phosphor layer as a function of time can easily be obtained through state-space analysis. Figure 23 is a contour plot of the space charge density in the phosphor layer of an ACTFEL device with dynamic space charge simulated assuming band-to-band impact ionization and subsequent hole trapping with a hole trap density of 5×10^{17} cm^{-3} and a hole trap depth of 0.7 eV, much like that simulated for Fig. 19 with the exception that for this simulation the phosphor layer was discretized into 101 layers so as to have 100 sheets of charge. When examining this plot it is important to note that the x-axis represents the depth into the phosphor layer with 0 being the anodic interface and 100 being the cathodic interface. Time is plotted on the y-axis starting at 0 μs and ending at 50 μs; 0 to 5 μs and 35 to 40 μs correspond to the rise and fall times of the applied voltage waveform, respectively, and 5 to 35 μs corresponds to the pulse width during which the maximum applied voltage is achieved. The space charge density is represented by the shading with the lightest areas having a density of less than 1×10^{10} cm^{-2} and the darkest areas having a density of greater than 2.5×10^{11} cm^{-2}.

The important features to note in Fig. 23 are as follows. First, note that initially (between 0 and 2 μs) there is no change in the space charge density at any position in the phosphor layer, but after that there is a slight decrease in the space charge density between the 60% and 100% positions in the phosphor layer. This decrease in space charge density corresponds to the decrease seen in Fig. 19 just prior to turn-on, which results from the increased internal fields caused by the application of the voltage pulse. Second, after the turn-on voltage has been reached and while electron injection is occurring from the cathodic interface (between 5 μs and 7 μs), there is a build-up in the space charge density near the center of the phosphor layer. While this may at first seem counterintuitive since the maximum space charge density might be expected to occur closer to the cathodic interface, this simulated trend may be reconciled with the fact that at the cathodic interface the phosphor fields

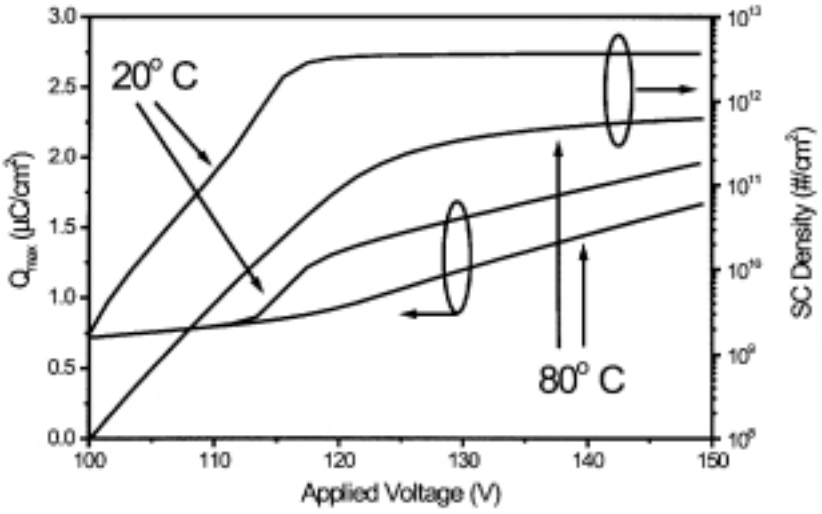

Figure 21: Simulated transferred charge and total space charge density curves for temperatures of 20° and 80°C. Note that the total space charge density at 80°C is less than the total space charge density at 20°C for all voltages. EL thermal quenching is attributed to this difference as with less space charge there is less of a cathode field enhancement, leading to a higher applied voltage required for threshold. These curves use identical parameters as in Fig. 20.

are higher so that any holes trapped in this region are emitted at a higher rate than in other phosphor regions, leading to a maximum space charge density which occurs near the phosphor center. Third, note that the space charge density in all regions decreases between 7 μs and 37 μs corresponding to the time period during which the applied voltage is sufficiently large to result in hole emission. Finally, note that for times greater than 37 μs, there is only a gradual decrease in space charge density as the phosphor fields decrease during the applied voltage rampdown (35 to 40 μs) to levels where the trap emission is low.

Another method of generating phosphor layer space charge is by impact ionization of deep electron traps. Figure 24 shows a contour plot of space charge density in the phosphor layer for a device where the dynamic space charge is assumed to result from the impact ionization of deep electron traps. For this simulation an electron trap density of 5×10^{15} cm^{-3} is used with a capture cross-section of 1×10^{-12} cm^2.

Figures 23 and 24 are dramatically different. Important features to note in Fig. 24 are first that prior to turn-on the region of maximum space charge density is the anodic interface, with space charge left from the previous (negative) pulse. Second, note that once turn-on occurs ($\sim$ 3 μs), the ionized traps at the anodic interface efficiently capture electrons which results in a rapid decrease in space charge density in that region. Also, although electrons are emitted from the cathodic interface (3 to 7 μs) there is a rapid build-up of positive space charge near the cathodic interface due to the ionized traps in this region not efficiently capturing electrons because of the high field that exists in this region. Finally, note that during the portion of the waveform where the applied voltage reaches its peak ($\sim$ 7 to 37 μs), electrons emitted from the cathodic interface can be captured throughout the phosphor layer, but most efficiently in the lower field regions nearer the anode.

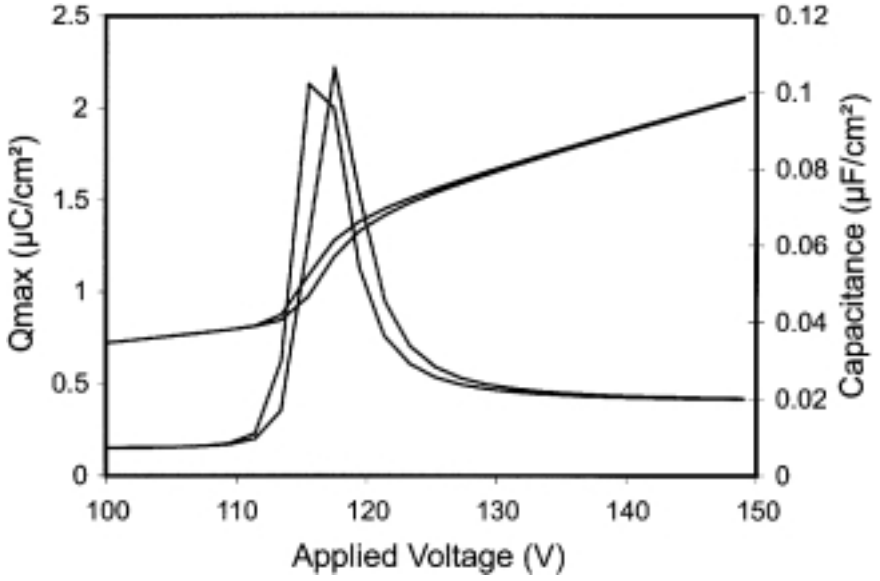

Figure 22: Simulated transferred charge and transferred charge capacitance curves for temperatures of 20° and 80°C. All parameters are identical to those used in Fig. 20 with the exception of the hole trap depth, which was increased to 1.0 eV. Note that the threshold voltages are nearly identical for these two simulations.

In summary, the most important trend evident from the contour plots shown in Figs. 23 and 24 involves the spacial and temporal nature of the positive space charge. The positive space charge concentration maximizes near the center of the phosphor layer when it is created by band-to-band impact ionization and hole trapping; also note that the region of positive space charge enhancement is relatively time invariant during a cycle of the applied voltage waveform. In contrast, as shown in Fig. 24, the positive space charge concentration varies periodically with the polarity of the applied voltage waveform and is always largest near the cathodic interface when the space charge is created through the impact ionization of deep electron traps. We believe Fig. 23 to be indicative of the space charge situation operative in a ZnS:Mn and perhaps a SrS:Cu ACTFEL device, whereas Fig. 24 is more illustrative of the operation of a SrS:Ce ACTFEL device.

6. State-Space ACTFEL Modeling Summary and Future

There are five significant advantages of state-space simulation: (1) the simplicity in the formulation of the basic state equations, (2) the ease in which state-space analysis can be automated, (3) the wealth of numerical techniques that exist to analyze equations in the state-space form, (4) the ease in which parasitic effects are implemented, and (5) the inherent decoupling of circuit and device physics effects in the simulation. As illustrated in the four examples presented in the previous subsection, state-space analysis is a powerful methodology for accomplishing realistic simulation of the internal physics of ACTFEL device operation as well as accounting for the test circuit parasitics that often play a dominant role in establishing measured trends.

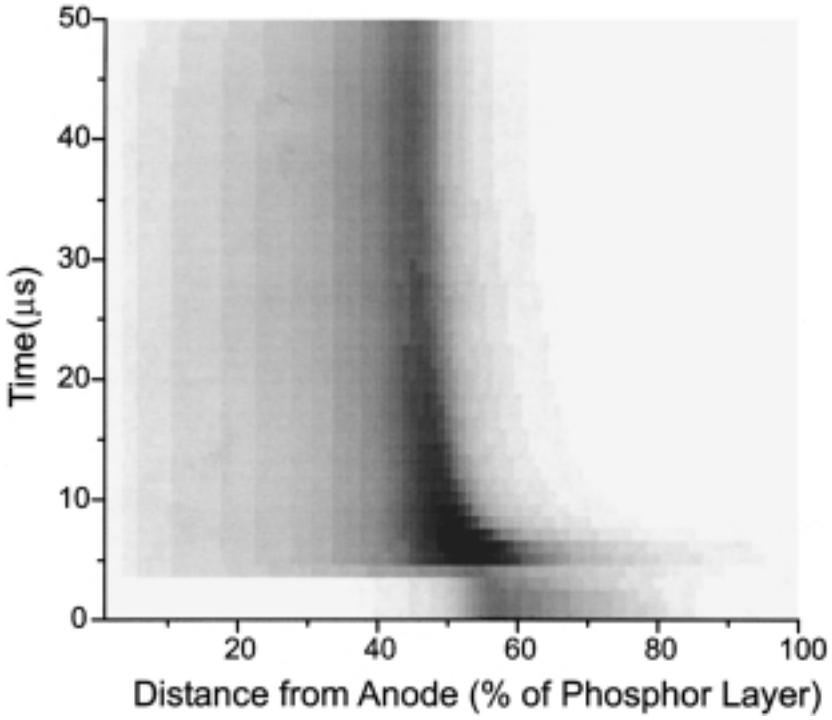

Figure 23: Space charge density as a function of both time and distance into the phosphor layer for the case of dynamic space charge resulting from band-to-band impact ionization and subsequent hole trapping. The shading corresponds to space charge density with no shading corresponding to a density of less than 10^{10} cm^{-2} and the darkest shading corresponding to a density of more than 2.5×10^{11} cm^{-2}.

There is, however, one very important physical process that has not yet successfully been implemented within the context of the state-space model. This involves the simulation of leakage charge, which is the charge that flows between pulses when the applied voltage is zero. Several approaches have been explored in an attempt to model leakage charge. One approach involves making the interface trap depth more shallow to provide leakage charge during the simulation. However, this leads to an unrealistically low turn-on voltage. A second approach to leakage charge modeling consists of employing many different formulations of phonon-assisted tunneling. A third approach involves the use of a shallow and a deep trap at the interface. A fourth approach attributes leakage charge to hole transport in the phosphor layer. All of these attempts to model leakage charge have proven unsuccessful. Currently, a leakage model involving emission from shallow electron traps in the phosphor layer is being investigated; initial results are promising.

Other enhancements to the ACTFEL state-space model that are expected in the near term are first, and most importantly, the addition of models accounting for the optical performance of these devices (i.e., luminescent impurity excitation, radiative recombination, and optical outcoupling). Inclusion of optical effects into the simulation will allow for true ACTFEL device electro-optic simulation. Issues such as the merits or demerits of having phosphor layer space charge present in an ACTFEL device may be explored within such a simulation environment. Another electrical characteristic that

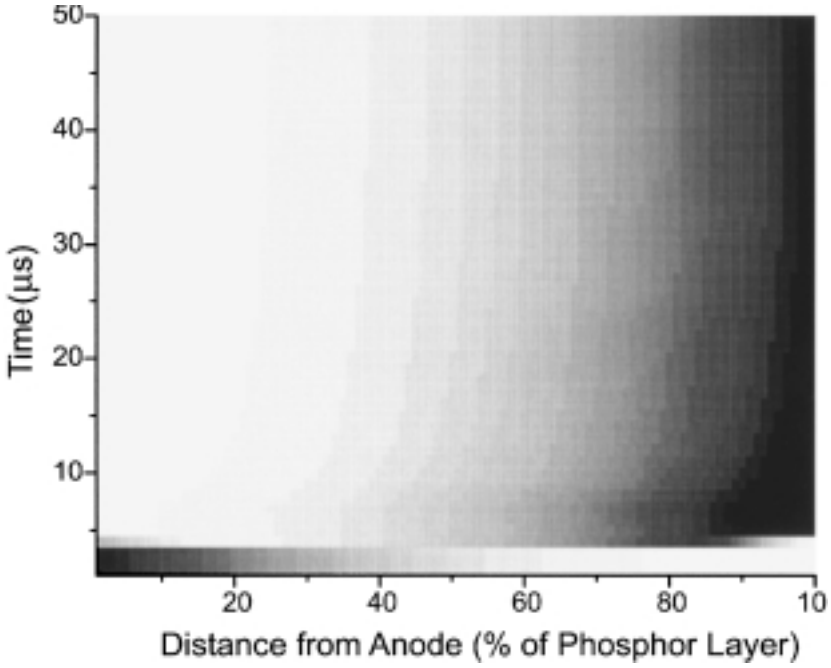

Figure 24: Space charge density as a function of both time and distance into the phosphor layer for the case of dynamic space charge resulting from trap-to-band impact ionization. The shading corresponds to space charge density with no shading corresponding to a density of less than 10^{10} cm^{-2} and the darkest shading corresponding to a density of more than 2.5×10^{11} cm^{-2}.

should be simulated is charge collapse, which is often seen in SrS:Ce devices [55]. Charge collapse is the movement of charge observed as the applied voltage pulse is ramping back to zero. Charge collapse is believed to result from the phosphor field at the anodic interface being reduced to such a low value that shallow traps at the anodic interface (or even electrons present in the conduction band) can emit during the fall time of an applied voltage pulse.

B. SPICE Modeling

Two primary topics are addressed in this section. First, a novel Fowler-Nordheim diode model for ACTFEL SPICE simulation is presented. This model is motivated by a recognition that Fowler-Nordheim tunneling is the dominant interface state electron emission mechanism. The Fowler-Nordheim diode model developed is appropriate for ACTFEL devices possessing negligible dynamic space charge. Using this model, excellent agreement is obtained between measured and simulated electrical characteristics of ZnS:Mn ACTFEL devices. Second, a SPICE realization of a two-sheet charge model is presented in which space charge generation is assumed to occur via tunneling from a discrete bulk trap. This model is capable of simulating manifestations of dynamic space charge generation such as C-V overshoot.

1. Fowler-Nordheim Diode Model

a. Derivation of a Basic Fowler-Nordheim Model The circuit topology of the basic Fowler-Nordheim model is shown in Fig. 25. The two capacitors, C_{it} and C_{ib}, represent the capacitances of the top and bottom insulators, respectively, as in previous SPICE-based models. In series with and sandwiched between these capacitors is a Fowler-Nordheim tunneling diode, which accounts for current transport across the phosphor. A "phosphor resistance," R_p, is added in parallel with the diode to account for charge leakage across the phosphor.

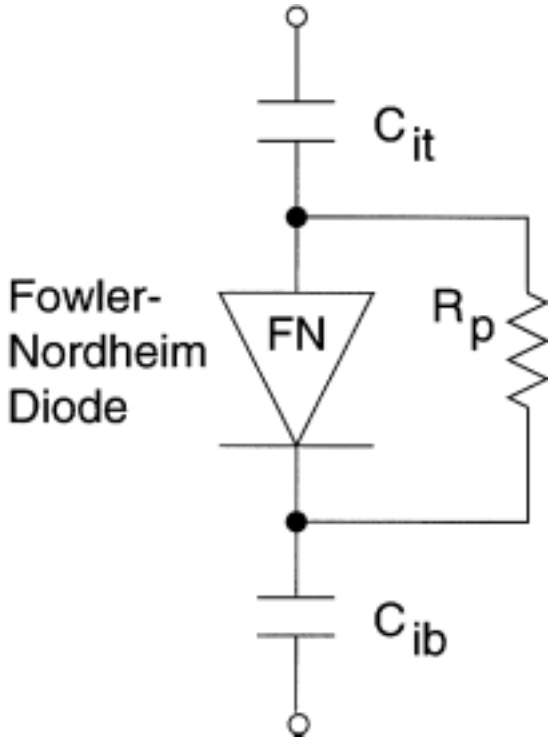

Figure 25: ACTFEL equivalent circuit using the SPICE Fowler-Nordheim diode model. Notice that the diode conducts under both applied voltage polarities.

The Fowler-Nordheim diode model is provided in HSPICE for modeling metal-insulator-semiconductor devices and consists of a voltage-dependent, non-linear current source in parallel with a fixed capacitance. The Fowler-Nordheim diode current-voltage characteristic is based on the equation for tunneling current through a triangular insulating barrier from a metal,

$$J_{FN} = \frac{q^2\mathcal{E}^2}{16\pi^2\frac{m^*}{m_0}\hbar\Phi_B}\exp\left[-\frac{4\sqrt{2m^*}(q\Phi_B)^{\frac{3}{2}}}{3q\hbar\mathcal{E}}\right] \tag{42}$$

where $\mathcal{E}$ is the electric field across the insulator, Φ_B is the metal-insulator barrier height in volts, and m^* is the effective mass of the tunneling carrier. Equation 42 is similar to Eq. (21) with the Coulombic barrier lowering factor ignored. Thus, the Fowler-Nordheim diode can be used to model this injection process in HSPICE, if appropriate substitutions are made: the metal-insulator barrier

height is replaced with the interfacial trap depth, the electric field across the insulator is replaced with the electric field across the phosphor, and the ZnS electron effective mass is used.

However, the Fowler-Nordheim HSPICE model characteristics are given in terms of lumped parameters useful for circuit engineering. In HSPICE, Eq. (42) appears as

$$id = A \cdot JF \cdot \left(\frac{v_d}{TOX}\right)^2 \exp\left[-\frac{EF \cdot TOX}{v_d}\right] \tag{43}$$

for forward applied biases, where A is the diode area, v_d is the voltage applied across the diode, TOX is the thickness of the "oxide," and JF and EF are lumped parameters called the forward current density and critical field, respectively. Initial experimentation made it clear that using these built-in SPICE parameters to model ACTFEL devices is unwieldy at best since the lumped parameters obscure the underlying physics. Therefore, it is necessary to relate the more familiar device physics quantities to the SPICE parameters using HSPICE's built-in algebraic features. To see how this is done, notice that Eqs. 42 and 43 are equivalent if

$$v_d = TOX \cdot \mathcal{E}, \tag{44}$$

$$EF = \frac{4\sqrt{2m^*}(q\Phi_B)^{\frac{3}{2}}}{3q\hbar}, \tag{45}$$

and

$$JF = \frac{q^2 m_0}{16\pi^2 m^* \hbar \Phi_B} \tag{46}$$

are chosen. Thus, the electron effective mass and interface trap depth are specified to characterize the model, and a software interface translates these to the necessary HSPICE parameters using equations following from Eqs. 44, 45, and 46. Analogous equations for the reverse-biased case (ER and JR) follow similarly.

Shunted across the voltage-controlled current source, the HSPICE Fowler-Nordheim model also includes a fixed capacitance whose value is

$$CD = \frac{\varepsilon_{OX}\varepsilon_0 A}{TOX}, \tag{47}$$

where ε_{OX} is the relative dielectric constant of silicon dioxide and ε_0 is the permittivity of free space. Unfortunately, the value of ε_{OX} is fixed in HSPICE and cannot be directly adjusted by the user to reflect materials other than silicon dioxide. However, a way to circumvent this limitation exists: the software interface adjusts the area parameter, A, so that the fixed capacitance is the same as it would be if ε_{OX} could be adjusted to the proper value. Then, the effect this adjustment to the area has on the current characteristics is offset by adjusting the JF parameter in the opposite direction, so that the current given by Eq. (43) remains unaffected.

b. Specification of Fowler-Nordheim Model Parameters Of the simulation parameters to be specified, most are known either from the literature and experimental circuit setup, or are determined from electrical characterization experiments or the processing parameters. The electron effective masses and the relative dielectric constants for a variety of phosphor materials have been reported in the literature. For ZnS, the electron effective mass has been reported to be 0.18 m_0 [71], and

the relative dielectric constant is 8.3. Important experimental circuit parameters to be included are the series resistance of the test setup and the parasitic oscilloscope resistance. The device area is a known process parameter.

The remaining non-adjustable parameters can be determined in two ways. First, the thicknesses of the phosphor and insulator layers are approximately known process parameters. These values, together with the device area and the dielectric constants of each layer, can be used to determine the insulator and phosphor capacitance values. However, due to uncertainty in the thickness values, better fits to data result when the parameters are derived from characterization experiments. Typically, the total device capacitance is measured from the pre-turn-on slope of either a Q-V plot or a maximum charge vs. maximum voltage (Q^{e}_{max}-V_{max}) plot, while the total insulator capacitance, $C_i = (C_{ib} \times C_{it})/(C_{ib} + C_{it})$, is measured from the post-turn-on slope of a Q-V or Q^{e}_{max}-V_{max} plot at 40 to 60 V over threshold. The phosphor thickness is determined using the measured phosphor capacitance value in conjunction with the phosphor dielectric constant and the insulator capacitance. The accuracy of the phosphor and insulator capacitances determined using either method is checked using the Q-F_p method: the Q-F_p plot of a ZnS:Mn device should be horizontal before turn-on during the rising portion of the waveform, and vertical after turn-on if the capacitance/thickness values are correct.

This leaves only two simulation parameters that need to be adjusted in order to obtain a good fit to experimental data: the interface trap depth and the value of the phosphor shunt resistance.

The interface trap depth is first adjusted until good agreement is obtained between experimental and simulated Q-V curves at a particular maximum applied voltage. Once the interface trap depth is optimized, the experimental and simulated Q-V curves are very similar, except that there is no leakage in the simulated Q-V curve. To account for leakage in the simulated curve, the phosphor shunt resistance is reduced from infinity to some finite value. Since higher leakage results in a reduced polarization field at the beginning of the next pulse, the turn-on is shifted slightly toward higher voltages for small values of the phosphor resistance; therefore, the interface trap depth value may need to be readjusted slightly after the leakage is accounted for through the addition of the phosphor resistor.

c. Results of Fowler Nordheim Model The accuracy of the Fowler-Nordheim diode model for a particular applied voltage is demonstrated in Fig. 26, which shows a Q-V curve of a 650 nm thick ZnS:Mn ACTFEL device driven 40 V over threshold at 1 kHz. The experimental curve and the simulated curve are seen to be very nearly coincident. The values of the interface trap depth and phosphor resistance used in the simulation are $\Phi_B = 1.03$ eV and $R_p = 0.65$ MΩ, respectively.

Figures 27 and 28 show the Q-F_p and C-V plots, respectively, which correspond to the Q-V plots in Fig. 26. The Q-F_p comparison between measured and simulated data shows that the model correctly accounts for the steady-state field and charge transfer in the ACTFEL device, whereas the C-V plots show the accuracy of the simulated turn-on voltage. Achieving a close fit for both the turn-on voltage and the conduction charge magnitude is fairly sensitive to model parameters; a good fit to one or the other is possible using a wide range of parameter values, but obtaining good fits to both simultaneously is more restrictive of the parameter set. For the model parameters shown in this section, a good fit to all data features is achieved, but the parameters are optimized with a preference to accurate transferred charge fits over more accurate turn-on voltage fits for several reasons. Mainly, a utility feature of this model is likely to be the prediction of ACTFEL power consumption, which is given by the area of a Q-V plot. Therefore, to better match the Q-V areas between simulation and

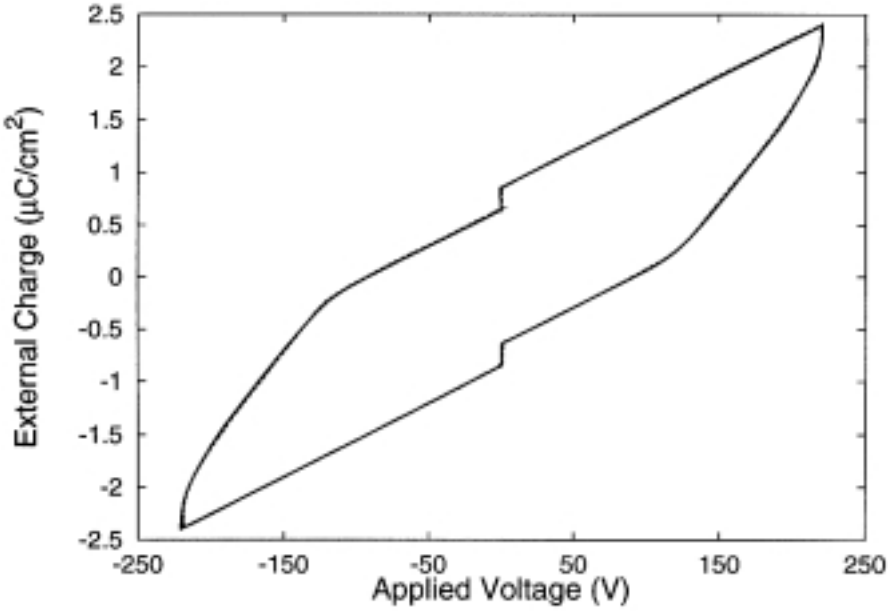

Figure 26: Q-V plot showing simulated (solid line) and measured (dashed line) data for an evaporated ZnS:Mn ACTFEL device driven 40 V over threshold at 1000 Hz.

measurement, the accuracy of the maximum transferred charge is expected to be somewhat more important than the accuracy of the turn-on fit.

Since the standard electrical measurements are parametric plots that do not explicitly reveal the transient dynamic response, it is conceivable that a model with excellent simulated Q-V agreement with measured data hypothetically could have poor agreement in the time domain. Simulated and measured transient charge [Q(t)] plots in Fig. 29 show that this is not the case for the model under consideration. The main limitations of the simulation are made more apparent in Fig. 29; however, the model turn-on is slightly more sluggish than an actual device, and this sluggishness must be compensated by a slightly more aggressive sourcing of charge during the plateau portion of the driving voltage pulse in order to transfer as much charge as a physical device by the end of the pulse. Second, the model exhibits less rounding in the Q(t) curve near the end of the fall portion of the pulse; this may simply be due to an RC effect of the experimental setup not accounted for in the model.

d. Scaling Model Parameters with Applied Voltage Figures 26 through 29 show excellent agreement between simulated and experimental data, but the model parameters used, which are optimized for a particular V_{max}, do not produce similarly good agreement at other V_{max}s.

The variation is easily seen in a Q^e_{max}-V_{max} plot. The dotted Q^e_{max}-V_{max} curve in Fig. 30 is produced using the same model that produces Figs. 26 through 29 — a basic Fowler-Nordheim diode model optimized for 40 V over threshold operation. Notice that the fit to the measured data is excellent at 40 V over threshold ($\sim$220 V), reasonably good at adjacent maximum voltages (especially higher voltages), and increasingly poor as the curves near threshold. Significantly, the simulated threshold is $\sim$ 40V below the experimental threshold and is much softer. If the simulation only needs

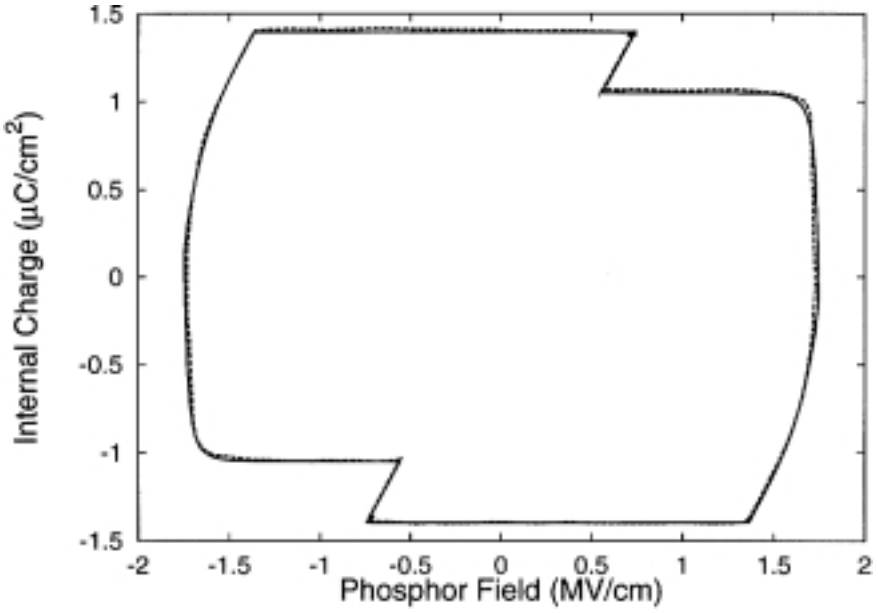

Figure 27: Q-F_p plot showing simulated (solid line) and measured (dashed line) data for an evaporated ZnS:Mn device driven 40 V over threshold at 1000 Hz.

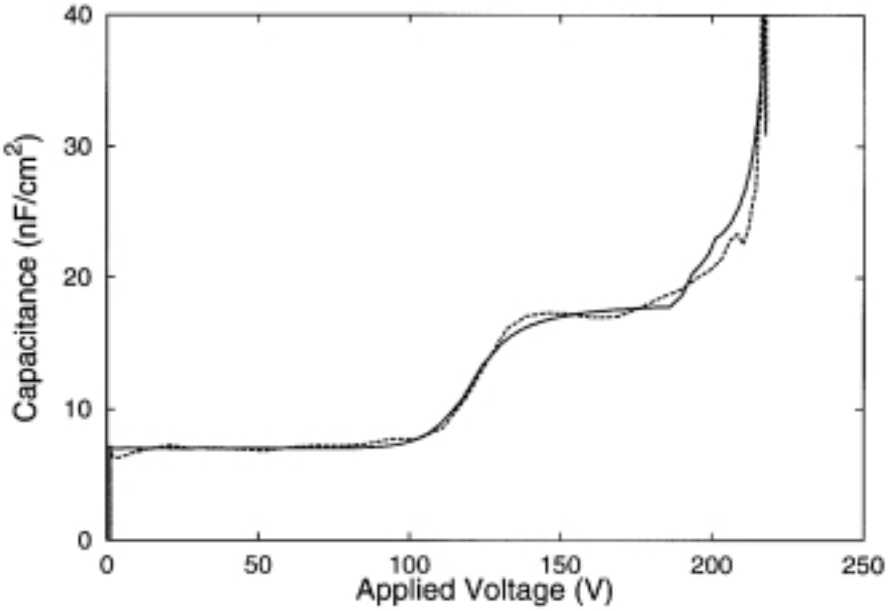

Figure 28: C-V plot showing simulated (solid line) and measured (dashed line) data for an evaporated ZnS:Mn device driven 40 V over threshold at 1000 Hz.

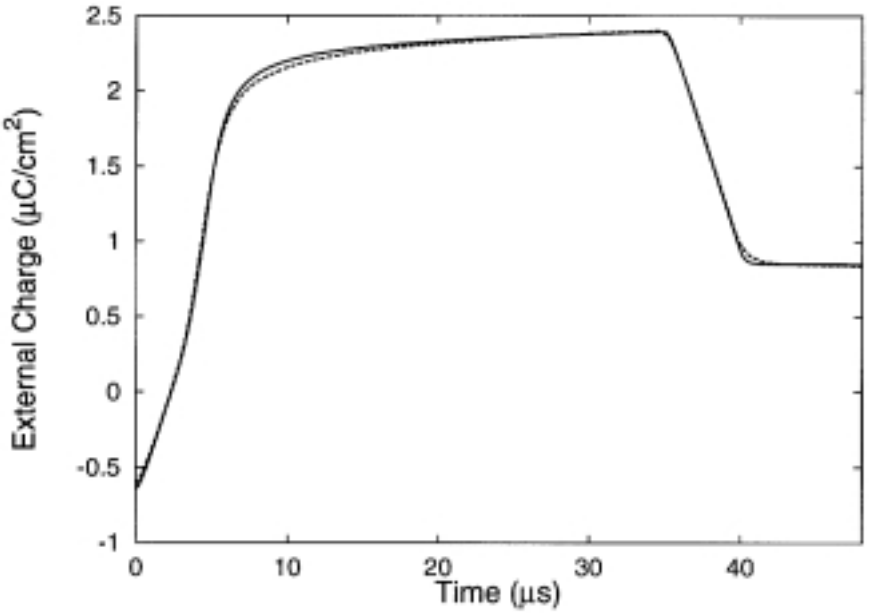

Figure 29: Transient charge plot showing simulated (solid line) and measured (dashed line) data. The device is driven 40 V over threshold at 1000 Hz.

to be accurate at high overvoltages (40 to 60 V over threshold), this model may suffice. However, it would be better to have a model that yields a close fit for any voltage.

To create such a model, the dependence of the best-fit values for the phosphor resistance and the interface trap depth on the overvoltage must first be determined. Figure 31 shows a plot of these best-fit values for a 650-nm thick ZnS:Mn operated at 1000 Hz as a function of overvoltage. The solid lines represent exponential fits to the data of the form

$$y = A\,\exp(-OV/\tau) + B \tag{48}$$

where y is either R_p or Φ_B and OV is the overvoltage. The parameters A, B, and τ in Eq. (48) are determined using least-squares estimation, yielding

$$\Phi_B = 0.1022\,\exp(-OV/16.956) + 1.0186 \tag{49}$$

and

$$R_p = 2.098\,\exp(-OV/14.288) + 0.4975. \tag{50}$$

Equations 49 and 50 present a very good fit to the best-fit parameter values, as seen in Fig. 31, especially considering the limited precision of the best-fit parameters. These equations are added to the basic model so that the trap depth and phosphor resistance decay exponentially when driven at voltages above threshold, resulting in the dashed line in the Q^e_{max}-V_{max} plot shown in Fig. 30.

The revised model is seen to present reasonable behavior above threshold. Two features of this curve are interesting, however. First, the post-threshold fit, although improved, is perhaps not as

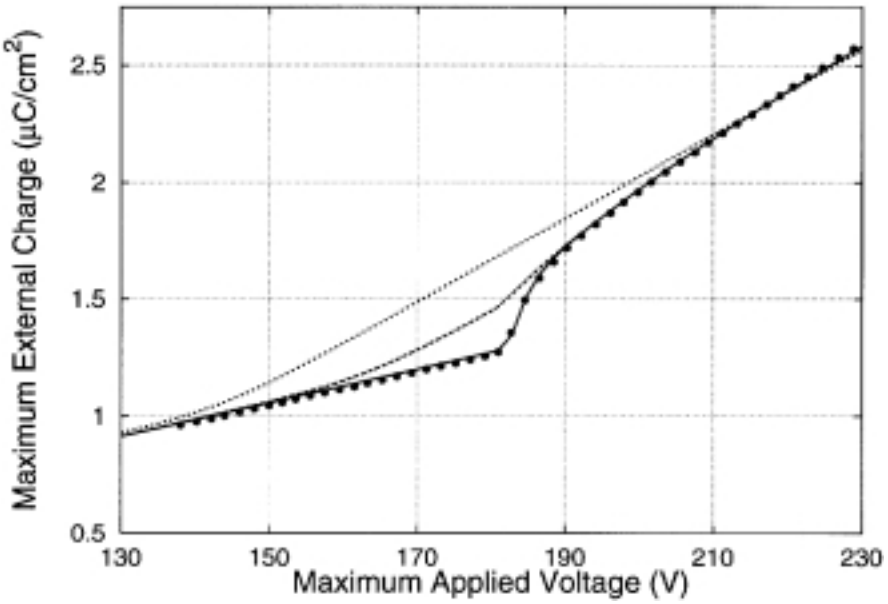

Figure 30: Q^e_{max}-V_{max} plot at 1000 Hz showing measured (dots) data and simulated data using three different Fowler-Nordheim-based SPICE models. The basic Fowler-Nordheim model (dotted line) is inadequate near and below threshold. Variation of the interface trap depth (dashed line) is seen to produce trends consistent with post-threshold device operation, while failing to reproduce turn-on trends. Adding a second exponential modulation to the model (solid line) results in better near-threshold behavior.

good as would be expected from Fig. 31. This is because the parameters (and thus the exponential fit) depend upon the overvoltage, but only the total applied voltage (i.e., the voltage applied across the series resistor, device, and sense capacitor) is available to the model. A possible solution to this problem would be to use the V_{max} value of the previous point to approximate the overvoltage of the next point, but this only makes sense in the context of a Q^e_{max}-V_{max} experiment. Other solutions would be to iteratively find the applied voltage, if accuracy is very important, or to assume a capacitive voltage divider in determining which fraction of the applied voltage falls across the device.

The second interesting feature of the dashed curve in Fig. 30 is the poor behavior below threshold. The value of Φ_B below threshold is fixed at approximately 1.12 eV by Eq. (49), whereas a minimum value of approximately 1.30 eV is required to adequately prevent the device from turning on before the desired threshold voltage. Therefore, a simple solution to the poor threshold fit is to simply add 0.18 eV to the trap depth below threshold. This solution is unsatisfying, though, due to a resultant discontinuity — the device turns on very abruptly so that the transferred charge capacitance is infinite at threshold. A better solution is to provide continuous behavior at threshold.

A number of methods may be used to accomplish this, but simply adding a second exponential function to Eq. (49) is easy and works well. Using

$$\Phi_B = 0.1022 \exp(-OV/16.956) + 1.0186 + 0.18 \exp(-OV/2) \tag{51}$$

in the model results in the solid line curve shown in Fig. 30, which exhibits reasonable near-threshold

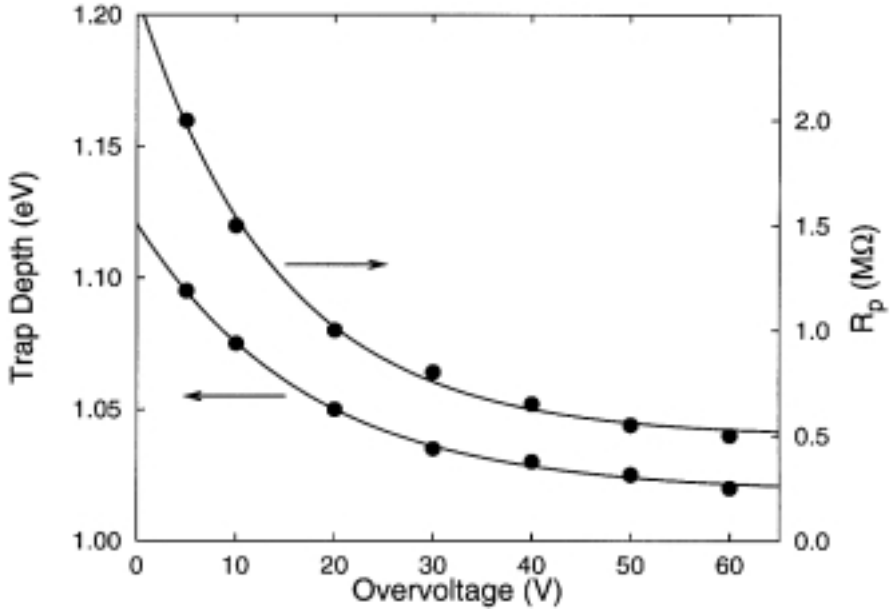

Figure 31: Trap depth and phosphor resistor (R_p) best-fit parameters for a 650-nm thick evaporated ZnS:Mn device operated at 1000 Hz. The points are the best-fit parameters and the curves show the least-squares best-fit exponential fit to the points.

and subthreshold behavior while maintaining post-threshold accuracy and providing a continuous-valued Φ_B at all voltages.

Finally, since slight adjustment of Φ_B and R_p leads to improved simulations, a brief discussion of some aspects of the physical nature of these parameters is warranted. First, consider the barrier height, Φ_B. Φ_B has been estimated as $\sim$1.5 eV from electrical characterization of ACTFEL devices with varying phosphor thicknesses [41, 70]. However, this calculation includes the effect of static space charge in the phosphor layer. In a physical device under excitation, the electric field near the cathode is higher than the average phosphor electric field due to the presence of static space charge throughout the phosphor, so that tunnel-emission from this interface is more efficient than the externally measured phosphor field would imply. However, space charge is not considered in the Fowler-Nordheim model shown in Fig. 25. Additionally, the built-in Fowler-Nordheim tunneling diode model current-voltage characteristic given in Eq. (42) does not include Coulombic barrier lowering effects. For both of these reasons, the interface state depth must be artificially lowered to the values shown in Fig. 31 in order to obtain a good fit to data in the simulations.

Next, consider the phosphor resistance, R_p. R_p should be regarded primarily as an adjustable parameter which quantitatively accounts for leakage charge in simulated Q-V curves. The physical significance of R_p (if any) is obscure. The resistivity of the ZnS phosphor has been reported as 10^8 to 10^{14} Ω·cm [72], corresponding to values of R_p ranging from 75 kΩ to 7.5×10^{10} Ω. While the best-fit value of R_p in the simulation is within this range, it is very doubtful whether this is in fact chiefly due to the low-field resistance of ZnS because of the uncertainty of the resistivity. Rather, the fact that the phosphor resistance value must be increased by a factor of 20 from the 1000 Hz best-fit values to fit 60 Hz values well argues strongly against this interpretation. R_p instead probably

accounts for trap emission via an unknown mechanism which is not included in the Fowler-Nordheim model.

2. Two-Sheet Charge Model

a. Device Physics–to–SPICE Mapping As mentioned in Section B., one approach to SPICE modeling is to first develop a device physics-based model, and then to map the device physics equations into corresponding dependent current sources in the SPICE model. This approach was pursued by Keir in mapping his single-sheet space charge model into SPICE as shown in Figs. 11 through 13 [48]. In this subsection, the single-sheet charge SPICE model is expanded into a two-sheet charge model.

In constructing the two-sheet charge model in SPICE, it is useful to refer to an energy band diagram of the ACTFEL device under forward bias, such as that shown in Fig. 32. Figure 32 shows two processes occurring in the ACTFEL device which need to be included in the model. The first is electron emission, both from the cathodic phosphor-insulator interface and from each sheet of charge. The second is electron recapture at the sheets of charge and the opposite interface.

As in the state-space model discussed previously, interface emission can occur via any of the three mechanisms in Section 2. and described by Eqs. 19, 21, and 22. However, the integral in Eq. (22) makes inclusion of phonon-assisted tunneling in a SPICE model difficult (an external program to calculate the emission rate and the incorporation of a look-up table in the SPICE program would be required), so only pure tunneling and thermal emission are included in the SPICE model. Thus, the total emission rate from an interface is just the sum of pure tunneling and thermal emission:

$$e_n = e_n^{PT} + e_n^{thermal}. \tag{52}$$

Except at very low fields, pure tunneling is expected to dominate the emission. The emission from the bulk sheets of charge is assumed to occur through field emission only, so that the $e^{thermal}$ term in Eq. (52) is omitted for bulk emission. Note that Eq. (52) gives the emission rate at an interface, as opposed to the emission current as in Eq. (42). Since the emission rate has units of inverse time, the emission current is given by

$$j_n = q n_x(t) e_n, \tag{53}$$

where $n_x(t)$ denotes the number of electrons per area available at the interface of interest, x, at a given time, t.

$n_x(t)$ must be known to use the emission rate to find the emission current. Note that at zero-field conditions, a certain number per unit area of electrons will be trapped at an interface. This number is termed the no-field occupancy, $N_0 f_0$, for the interfaces, and the number of traps, N_T, for the bulk sheets of space charge. The number of the electrons available at the interface or bulk trap will decrease as emission occurs. Thus, the number of electrons per area present at interface x is the sum of the electrons present under zero-field conditions minus the number which have been emitted:

$$n_x(t) = N_0 f_0^x - q_x(t)/(-q), \tag{54}$$

where q_x is the amount of emitted charge per area, $-q$ is the charge of an electron, and N_T is substituted for $N_0 f_0$ in the case of a bulk trap. (A positive value of q_x therefore corresponds to excess trapped electrons.) q_x can be found by applying Gauss' Law. For instance, the amount of

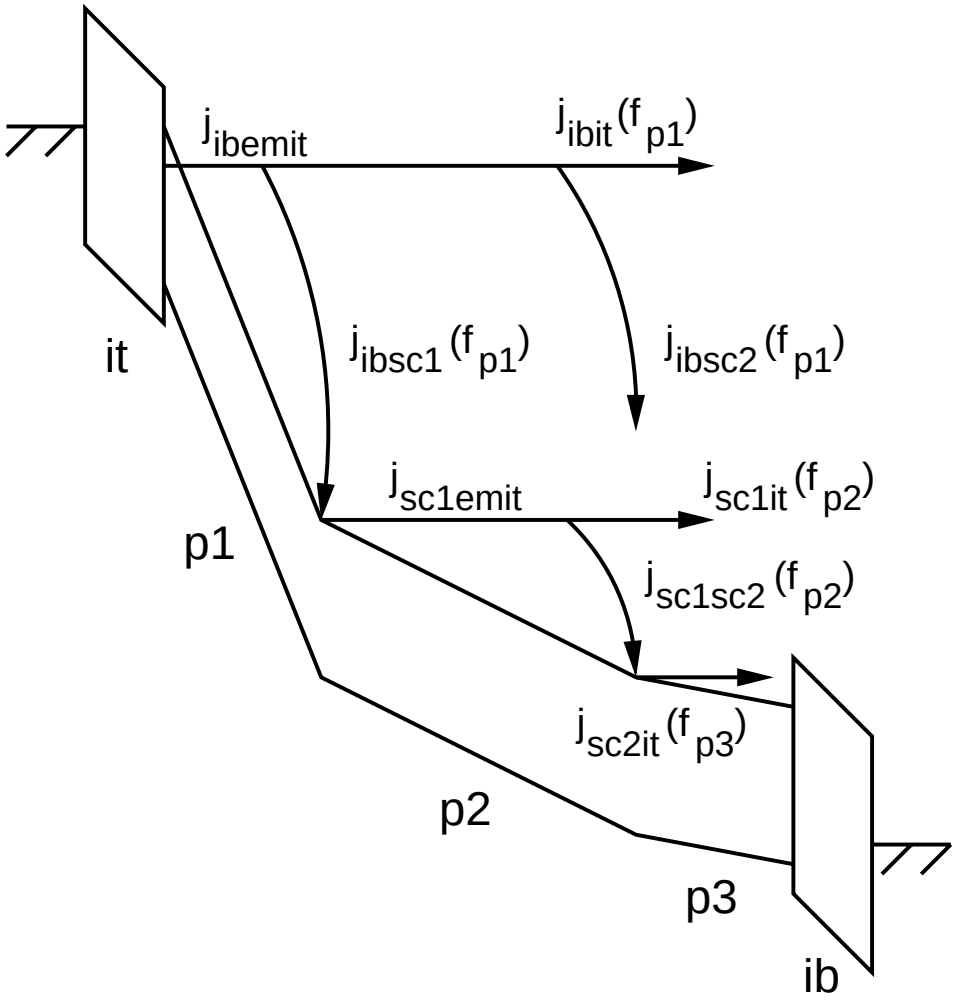

Figure 32: Energy band diagram representation of the conduction and space charge currents for an ACTFEL device in which space charge creation is limited to two discrete sheets in the phosphor bulk.

charge per area emitted from the bottom interface, q_{ib}, and from the first sheet of space charge, q_{sc1}, is given by

$$-q_{ib}(t) = C_{ib}v_{ib}(t) - C_{p1}v_{p1}(t) \tag{55}$$

and

$$-q_{sc1}(t) = C_{p1}v_{p1}(t) - C_{p2}v_{p2}(t), \tag{56}$$

where the Cs refer to the normalized capacitances of each layer and the vs refer to the voltage dropped across the layer. Similar equations follow for q_{sc2} and q_{it}. These equations are then inserted into Eq. (54) to give $n_{ib}(t)$, $n_{sc1}(t)$, and so forth.

Next, the probability of electron capture by each trap must be included. First, any electron reaching either phosphor-insulator interface is trapped at the interface. In addition, an electron has a finite chance to be trapped at any sheet of charge it must traverse on its way to an interface. This probability is termed the space charge capture factor for trap x, $sccf_x$, and varies between 0 and 1. Several possibilities for the formulation of $sccf_x$ are possible. The simplest is to simply assign a constant value, which can be fit to experimental data. However, electron capture is affected by two conditions. The first of these is the electric field strength at the trap: capture is much more likely for a trap in a low field than a high field. One formulation used by Bouchard et al. assumed the capture probability varied linearly with field, as in

$$sccf_x(f_p) \propto \left(1 - \left|\frac{f_p}{f_{0c}}\right|\right), \tag{57}$$

where f_{0c} is the critical field above which capture is not allowed, and f_p is taken as the average of the two phosphor fields existing on either side of the sheet of charge [53]. The second condition affecting electron capture at a bulk trap is the occupancy of the trap. Logically, the probability of capture should increase as the proportion of unfilled to filled traps increases. Additionally, device physics-based space charge modeling efforts typically assume the space charge is positive and preclude the possibility of negative space charge; in other words, the bulk traps cannot hold more electrons than in the no-field situation. Bouchard et al. account for both aspects of this second condition by multiplying Eq. (57) by an additional term, so that

$$sccf_x(f_p) = \left(1 - \frac{n_x}{N_t}\right)\left(1 - \left|\frac{f_p}{f_{0c}}\right|\right), \tag{58}$$

where n_x is given by Eq. (54). As will be seen later, the number of electrons emitted from the trap relative to the total number available is quite small, so that the first term of Eq. (58), $(1 - n_x/N_t)$, approaches zero and thus forces the total capture factor towards zero. To counteract this effect, Eq. (58) is modified to

$$sccf_x(f_p) = \left[1 - \left(\frac{n_x}{N_t}\right)^y\right]\left(1 - \left|\frac{f_p}{f_{0c}}\right|\right). \tag{59}$$

If y is specified large enough, the main effect of the first term of Eq. (59) is to limit the occupancy of the trap to N_t but otherwise does not significantly affect the value of $sccf_x$. For small values of y, the occupancy of the trap becomes more important, but the overall value of $sccf_x$ is likely to be small and the trap will never be completely refilled. For the simulation results presented in the next subsection, $y = 250$ so that the former condition holds.

Now that the treatment of both emission and electron recapture has been described, the mapping of these processes into a SPICE model can proceed. Again referring to Fig. 32, notice that the ACTFEL device is divided into five regions: two insulators and three segments of phosphors separated by the two sheets of charge. These regions are first mapped as the five capacitors shown in Fig. 33, whose capacitance values are simply determined from the device area, the dielectric constants of the phosphor and insulator materials, and the thickness of each region. Next, each electron flux shown in Fig. 32 is mapped to the correspondingly named dependent current source in Fig. 33, noting that the polarity of the current sources is opposite that of the electron flux. Next, the mathematical characteristics of each current source are defined. The total electron emission current from the interface and each sheet of charge is given by Eq. (53) with the appropriate occupancy and field

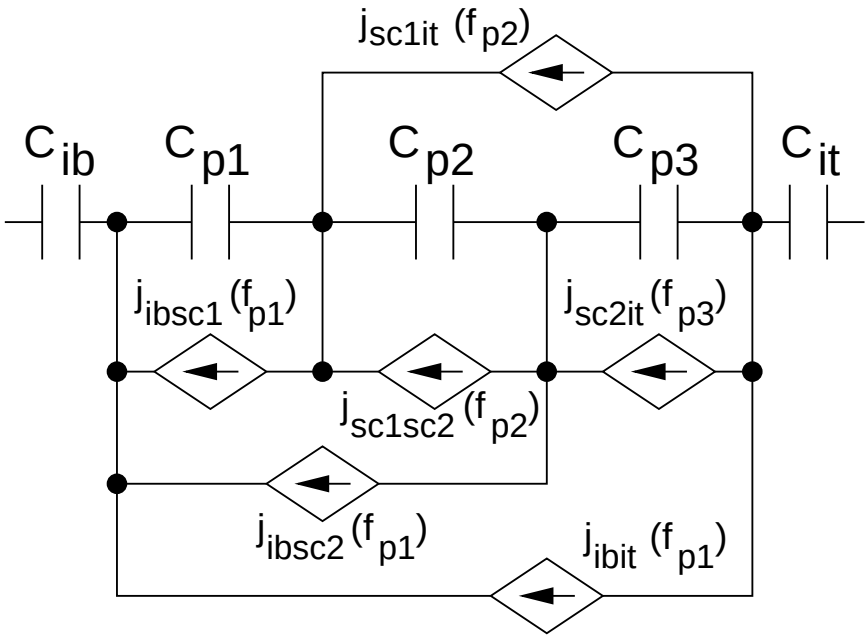

Figure 33: Equivalent circuit model for the two-sheet charge model under forward bias, in which the three emission and three space charge capture currents shown in Fig. 32 are represented by six voltage-controlled dependent current sources.

terms substituted in. The emission current density from the second charge sheet appears directly in Fig. 33. However, some portion of the electrons originating at the interface and first charge sheet are trapped within the bulk and do not reach the anodic interface. Subtracting out the trapped electrons, it can be shown that

$$j_{ibsc1} = j_{ibemit}(f_{p1}) \cdot sccf_1, \tag{60}$$

$$j_{ibsc2} = j_{ibemit}(f_{p1}) \cdot (1 - sccf_1) \cdot sccf_2, \tag{61}$$

$$j_{ibit} = j_{ibemit}(f_{p1}) \cdot (1 - sccf_1) \cdot (1 - sccf_2), \tag{62}$$

$$j_{sc1sc2} = j_{sc1emit}(f_{p2}) \cdot sccf_2, \tag{63}$$

and

$$j_{sc1it} = j_{sc1emit}(f_{p2}) \cdot (1 - sccf_2). \tag{64}$$

Finally, the mapping process is repeated for the negative polarity of the applied voltage pulse to complete the model. Note that each applied voltage pulse polarity requires the use of 6 voltage-dependent current sources so that a total of 12 are required in the final model.

b. SPICE Two-Sheet Charge Model Simulation Results The most obvious benefit of the two-sheet charge model is the ability to model symmetric and asymmetric capacitance overshoot. Figure 34 shows the C-V characteristics for the 12 current source models described in the previous

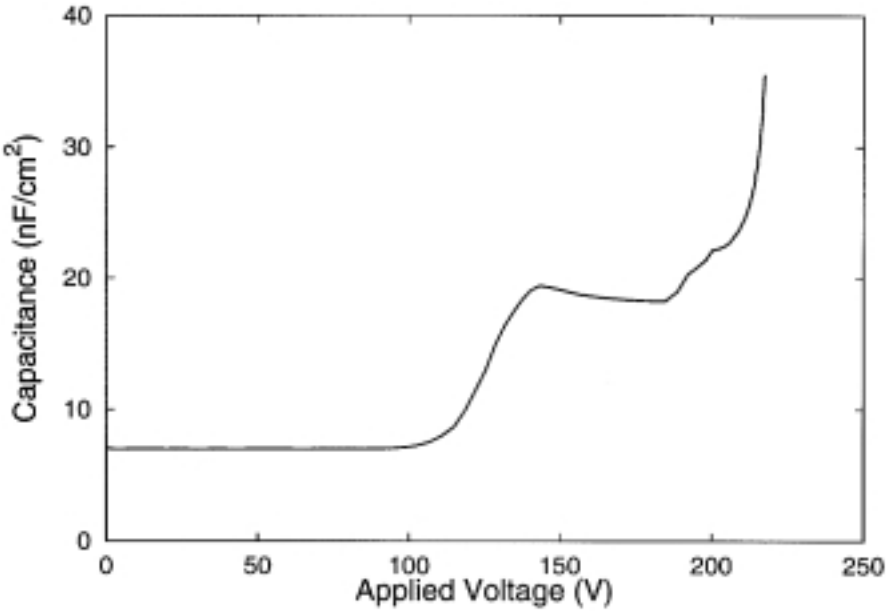

Figure 34: C-V plot showing capacitance overshoot in the two-sheet charge model with space charge creation via field emission. This overshoot is present for both applied voltage polarities.

subsection, using the parameters listed in Table 2. Only the positive polarity is shown since the negative polarity C-V curve is identical for the parameters simulated. The amount of overshoot seen in Fig. 34 is only moderate, as is typical when space charge creation is assumed to occur via field emission [48, 53]. The model may be made to yield asymmetric overshoot by adjusting the simulation so that different parameter values are used for each sheet of charge.

Table 2: Nominal ACTFEL double sheet-charge SPICE simulation parameters.

Simulation Parameter	Value	Simulation Parameter	Value
Phosphor Thickness	650 nm	Interface Trap Depth	1.30 eV
Phosphor Dielectric Constant	8.3	Space Charge Trap Depth	1.25 eV
Total Insulator Capacitance	18 nF/cm^2	Electron Relative Effective Mass	0.18
Device Area	0.085 cm^2	Neutral Interface Trap Density	5×10^{13} cm^{-2}
Charge Sheet Distance from Interfaces	50 nm	Bulk Trap Density	5×10^{13} cm^{-2}
Rise Time	5 μs	Electron Capture Critical Field	2 MV/cm
Pulse Width	30 μs	Thermal Emission Cross Section	1×10^{-15} cm^2
Fall Time	5 μs	Temperature	300 K
Frequency	1000 Hz	Series Resistance	500 Ω
Cycles Simulated	3	Sense Capacitance	109.0 nF

Careful observation of Fig. 34 reveals another important result of the SPICE two-sheet charge model. Inclusion of the series resistance in the test circuit leads to a “bump” in the C-V curve near 200 V. Such a C-V “bump” is also evident in state-space simulation, as discussed in Section 5. and is often observed experimentally, if the signal-to-noise ratio is adequate in this portion of the C-V

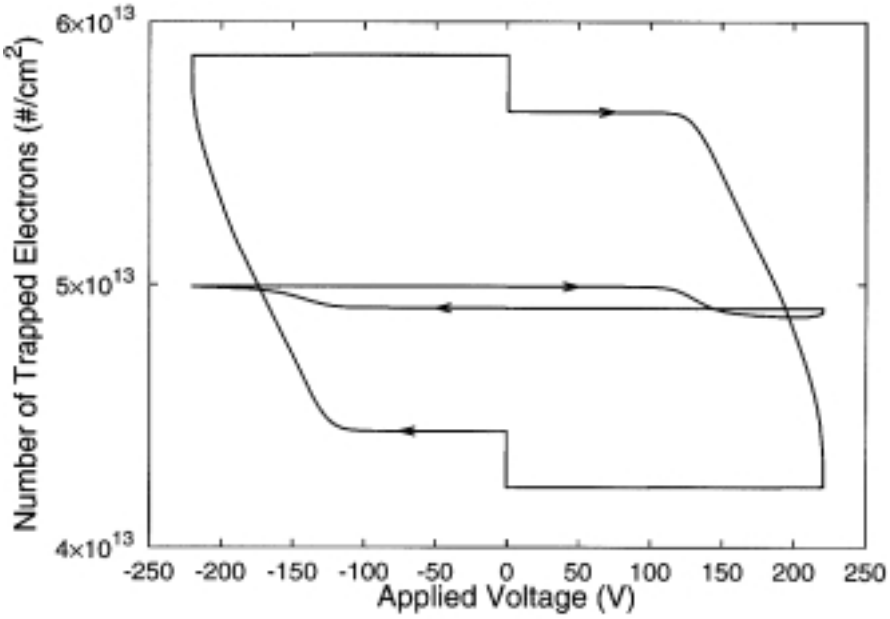

Figure 35: Plot showing the occupancy of the bottom insulator-phosphor interface (outer curve) and the first sheet of charge (inner curve). $N_0 f_0$ and N_T are both 5×10^{13} cm^{-2}.

curve. Including this series resistance and the oscilloscope resistance is trivial in SPICE, but was found to be very difficult in a device physics modeling framework [53].

Figure 35 shows the occupancy of the bottom phosphor-insulator interface (outer curve) and the first sheet of charge (i.e., the charge sheet near the bottom interface; inner curve), which is instructive in elucidating the internal working of the model. First, note that both $N_0 f_0$ and N_T are set to 5×10^{13} cm^{-2}, as noted in Table 2. At the beginning of a positive pulse, the occupancy of the bottom interface is higher than this number, due to the accumulation of electrons emitted from the top interface during the previous negative half-cycle. As the applied voltage is ramped past the turn-on voltage, the interface begins to emit electrons, and the number of trapped electrons decreases to a minimum at the end of the applied pulse. The trap is then refilled through a combination of charge leakage from the top interface and electrons emitted from the top interface or sheets of charge during the negative portion of the applied voltage waveform. As seen in Fig. 35, electrons begin to be emitted from the first charge sheet approximately at the same time as interfacial emission begins. This "extra" emission, which is not expected in a device without space charge, is responsible for the overshoot seen in C-V characteristics. Note that it is possible for charge emitted from the bottom interface to be trapped at the first charge sheet during this time, but the probability is very small due primarily to the high field near the sheet of charge. However, notice that the occupancy of the first sheet of charge increases during the positive voltage pulse plateau portion of the waveform; this increase is a consequence of the flow of relaxation charge which reduces the field, which in turn increases the space charge capture factor. The traps in the first charge sheet are refilled during the negative portion of the applied voltage waveform by electrons emitted from the top interface or from the second sheet of charge. Finally, notice that the occupancy of the bulk trap does not exceed N_T as

that of the interfacial trap exceeds $N_0 f_0$. In fact, depending on the value specified for the critical field for electron capture, or other simulation parameters, the charge sheet does not necessarily have to be refilled completely. Rather, a certain number of traps are unfilled at all times during the waveform. The positive space charge present due to these permanently unfilled traps could be used to simulate static space charge. For the simulation shown in Fig. 35, the parameters are set so that the charge sheet is fully refilled in order to increase the amount of C-V overshoot.

The equivalent circuit for the SPICE two-sheet charge model shown in Fig. 33 is appropriate for the most general case; that is, all possible connections between different phosphor nodes are established and appropriate mathematical relationships between them are modeled using voltage-dependent current sources. This is appropriate in device physics modeling, where the simulations should reflect physical reality as much as possible. However, each additional current source that is included in the SPICE model increases the simulation time. Therefore, it may be desirable to create a simpler two-sheet charge model by eliminating unnecessary current sources from Fig. 33. As seen from Fig. 35, the role that cathodic phosphor-insulator interface emission plays in refilling the traps in the closest sheet of charge is minor due to the high field in this region; thus, j_{ibsc1} can be eliminated. Since the number of electrons emitted from bulk traps is much smaller than the number emitted from interfaces, the role that these electrons play in refilling the other sheet of charge is also small; therefore, j_{sc1sc2} can be removed. Finally, since the sheet of charge located closest to the anode is expected to be in a low-field region, emission from that sheet is likely to be small, and j_{sc2it} can be omitted. Three sources are left, which are required for proper operation of the model: j_{ibit} accounts for most of the conduction charge, j_{sc1it} accounts for C-V overshoot, and j_{ibsc2} is needed to refill the second charge sheet. Repeating the elimination process for the other applied voltage polarity leads to a model that has only 6 current sources, reduced from 12.

C-V plots produced using this simplified six-current source model are shown in Fig. 36. Curve (a) exhibits a similar amount of overshoot to that shown in Fig. 34, yet this model requires only one-third of the computing time as the 12-source model. Curve (a) uses a field-dependent space charge capture factor and does not allow negative space charge. Eliminating the stipulation that no negative space charge be allowed results in a modest computer time savings, as the current source equations are simplified. This has the added benefit of increasing the amount of C-V overshoot, since more charge is available at the cathodic charge sheet to be emitted, as seen in curve (b) of Fig. 36. Note that Fig. 36(b) exhibits a reduced slope at the onset of turn-on, which can be understood in terms of the following. The excess electrons trapped at the "overfull" sheet of charge result in the energy bands being pushed upward compared to the limited-occupancy case, which serves both to reduce the field at the cathodic interface and to increase the field at the sheet of charge. Thus, electron emission from the interface is more difficult than before, while emission from the sheet of charge is easier. Thus, the sheet of charge now begins emitting electrons before the interface does. A similar effect is seen when the trap depth at the sheets of charge are specified as significantly lower than the trap depth at the interfaces. Finally, the space charge capture factor can be replaced by a constant, resulting in a model that simulates in only one-sixth the time of the original 12-current source model. For $sccf = 0.15$, curve (c) in Fig. 36 results.

3. SPICE ACTFEL Modeling Summary and Future

ACTFEL SPICE modeling offers a number of advantages. First, the inclusion of external circuitry, such as driver electronics, parasitic effects, or series resistors, is easily accomplished. This makes SPICE models ideal for circuit engineering or power estimation applications. Second, the mathe-

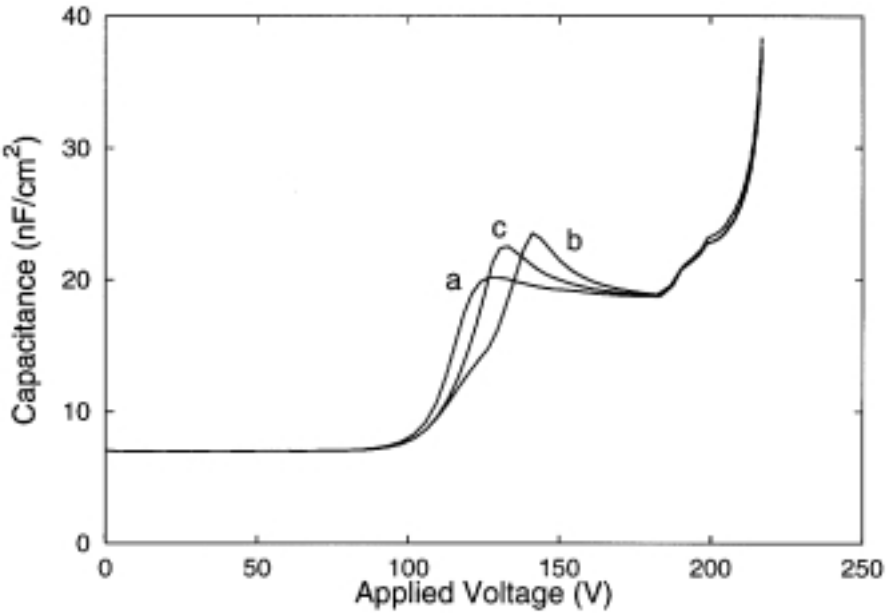

Figure 36: C-V plots showing capacitance overshoot in simplified six-current source two-sheet charge models. The models that produce these curves differ only in the handling of the charge capture coefficient. The model that produces curve (a) uses a field-dependent space charge capture factor and does not allow negative space charge. Curve (b) is similar to (a), except negative space charge is allowed in the model. Curve (c) results when a constant capture factor $sccf = 0.15$ is used.

matical solution of the model is largely handled automatically by the SPICE program, decoupling the formulation of the model from the computation. Third, as illustrated by the Fowler-Nordheim diode ACTFEL model example, relatively simple models can simulate ZnS:Mn ACTFEL devices with excellent accuracy while requiring minimal computer time. Finally, the two-sheet charge SPICE model demonstrates that much of the device physics-based modeling work can also be implemented in a SPICE environment, blending the power of this modeling approach with the convenience of SPICE to circuit engineers.

A number of enhancements to both the Fowler-Nordheim and two-sheet charge SPICE models are planned for the near future. First, the frequency dependence of the Fowler-Nordheim model parameters, specifically of the phosphor resistance, will be included in a manner analogous to the modeling of the overvoltage dependence. Second, the two-sheet charge model will be expanded to include trap-to-band impact ionization as a possible space charge creation mechanism. Next, as in the state-space model, optical models are to be included in both SPICE models to allow for simulation of the optical performance of ACTFEL devices as well as the electrical characteristics.

IV. Conclusions

The primary objective of the modeling efforts reviewed herein is to accurately simulate the electrical properties of two-terminal ACTFEL test structures when subjected to realistic applied voltage waveforms. Previous ACTFEL device physics modeling work is reviewed. Additionally, n-sheet state-space and SPICE simulation are described since they constitute powerful and complementary routes to ACTFEL modeling. Future state-space ACTFEL modeling challenges include accounting for leakage charge and charge collapse. Future SPICE simulation work includes extending the Fowler-Nordheim model to account for frequency-dependent effects and expanding the two-sheet charge model to include trap-to-band impact ionization as a possible space charge creation mechanism. The most important necessary embellishment of future state-space and SPICE models is to simulate the optical performance of ACTFEL devices. Inclusion of optical effects will allow for full electro-optic simulation of the ACTFEL devices. Finally, an effort should be made to model hetero-phosphor ACTFEL devices, which have two or more phosphor layers composed of different materials in order to produce white light. These white devices may prove important in the construction of full-color displays.

Acknowledgments

This work was supported by the U.S. Army Research Office under Contract no. DAAL03-91G0242 and DAAH04-94-G-0324, the Defense Advanced Research Projects Agency under MDA 972-94-C-0023, and the Phosphor Technology Center of Excellence, Grant No. MDA 972-93-1-0030.

References

[1] **Ono, Y. A.,** *Electroluminescent Displays*, World Scientific, Singapore, 1995.

[2] **Shionoya, S. and Yen, W. M.,** *Phosphor Handbook*, CRC Press, Boca Raton, FL, 1999.

[3] **Bringuier, E.,** *J. Appl. Phys.*, 70, 4505, 1991.

[4] **Bringuier, E. and Bhattachayyra, K.,** *Semi. Sci. Technol.*, 10, 1065, 1995.

[5] **Bringuier, E.,** *J. Appl. Phys.*, 75, 4291, 1994.

[6] **Dür, M., Goodnick, S. M., Shankar, S., Wager, J. F., Reigrotzki, M., and Redmer, R.,** *J. Appl. Phys.*, 83, 3176, 1998.

[7] **Blasse, G. and Grabmaier, B. C.,** *Luminescent Materials*, Springer-Verlag, Berlin, 1994.

[8] **Ylilammi, M.,** *J. SID*, 3, 59, 1995.

[9] **Brennan, K.,** *J. Appl. Phys.*, 64, 4024, 1988.

[10] **Bhattachayyra, K., Goodnick, S. M., and Wager, J. F.,** *J. Appl. Phys.*, 73, 3390, 1993.

[11] **Åberg, M.,** Ph.D. Thesis, Helsinki University of Technology, Helsinki, Finland, 1993.

[12] **Beck, D. R., Wager, J. F., Arbuthnot, L., and Flegal, T.,** *SID 97 Digest*, 615, 1997.

[13] **Beck, D. R.,** M.S. Thesis, Oregon State University, 1997.

[14] **Chen, Y. S. and Krupka, D. C.,** *J. Appl. Phys.*, 43, 4089, 1972.

[15] **Smith, D. H.,** *J. Lumin.*, 23, 209, 1981.

[16] **Howard, W. E., Sahni, O., and Alt, P. M.,** *J. Appl. Phys.*, 53, 639, 1982.

[17] **Alt, P. M.,** *Proc. SID*, 25, 123, 1984.

[18] **Bringuier, E.,** *J. Appl. Phys.*, 66, 1314, 1989.

[19] **Bringuier, E.,** *J. Appl. Phys.*, 67, 7040, 1990.

[20] **Ylilammi, M.,** *IEEE Trans. Electron Devices*, ED-42, 1227, 1995.

[21] **Tanaka, S., Yoshiyama, H., Mikami, Y., Nishiura, J., Ohshio, S., and Kobayashi, H.,** *Proc. SID*, 29, 77, 1988.

[22] **Singh, V. P. and Morton, D. C.,** *IEEE Trans. Electron Dev.*, ED-36, 54, 1989.

[23] **Geoffroy, A. and Bringuier, E.,** *Semicond. Sci. Technol.*, 6, A131, 1991.

[24] **Bringuier, E. and Geoffroy, A.,** *Appl. Phys. Lett.*, 60, 1256, 1992.

[25] **Douglas, A. A., Wager, J. F., Morton, D. C., Koh, J., Hogh, C. P.,** *J. Appl. Phys.*, 73, 296, 1993.

[26] **Abu-Dayah, A., Kobayashi, S., Wager, J. F.,** *J. Appl. Phys.*, 74, 5575, 1993.

[27] **Ohmi, K., Inoue, S., Tanaka, S., and Kobayashi, H.** *Appl. Phys. Lett.*, 64, 3464, 1994.

[28] **Neyts, K. A., Corlatan, D., De Visschere, P., and Van den Bossche, J.,** *J. Appl. Phys.*, 75, 5339, 1994.

[29] **Abu-Dayah, A. and Wager, J. F.,** *J. Appl. Phys.*, 75, 3593, 1994.

[30] **Corlatan, D., Neyts, K. A., and De Visschere, P.,** *J. Appl. Phys.*, 78, 7259, 1995.

[31] **Neyts, K. A. and Soininen, E.,** *IEEE Trans. Electron Dev.*, ED-42, 1086, 1995.

[32] **Ohmi, K., Ishitani, K.,Tanaka, S., and Kobayashi, H.,** *Appl. Phys. Lett.*, 67, 944, 1995.

[33] **Ang, W. M., Pennathur, S., Pham, L., Wager, J. F., Goodnick, S. M., Douglas, A. A.,** *J. Appl. Phys.*, 77, 2719, 1995.

[34] **Shih, S., Keir, P. D., Wager, J. F., Viljanen, J.,** *J. Appl. Phys.* 78, 5775, 1995.

[35] **Thuemler, R. L., Wager, J. F.,** *SID 95 Digest*, 473, 1995.

[36] **Neyts, K. A.,** *IEEE Trans. Electron Dev.*, ED-43, 1343, 1996.

[37] **Ohmi, K., Ishitani, K., Kashio, Y., Fujimoto, Y., Tanaka, S., and Kobayashi, H.,** presented at the *Second International Conference on the Science and Technology of Display Phosphors*, San Diego, CA, November 18-20, 1996.

[38] **Neyts, K. A., Corlatan, D., De Visschere, P., Lahonen, M., and Viljanen, J.,** *J. SID*, 5, 137, 1997.

[39] **Wager, J. F. and Keir, P. D.,** *Ann. Rev. Mater. Sci.*, 27, 223, 1997.

[40] **Meyers, R. and Wager, J. F.,** *J. Appl. Phys.*, 81, 506, 1997.

[41] **Hitt, J. C., Keir, P. D., and Wager, J. F.,** *J. Appl. Phys.*, 83, 1141, 1998.

[42] **Neyts, K. A. and De Visschere, P.,** *J. Appl. Phys.*, 68, 4163, 1990.

[43] **Neyts, K. A.,** *IEEE Trans. Electron Dev.*, ED-38, 2604, 1991.

[44] **Singh, V. P., Krishna, S., Morton, D. C.,** *J. Appl. Phys.*, 70, 1811, 1991.

[45] **Singh, V. P., Majid, W. Z., and Morton, D. C.,** *Conference Record of the 1991 International Display Research Conference*, 1991, 130.

[46] **Singh, V. P., Majid, W. Z., and Morton, D. C.,** *J. SID*, 1, 135, 1993.

[47] **Keir, P. D., Ang, W. M., Wager, J. F.,** *J. Appl. Phys.*, 78, 4668, 1995.

[48] **Keir, P. D.,** M.S. Thesis, Oregon State University, 1995.

[49] **Keir, P. D., Ang, W. M., Wager, J. F.,** *SID 95 Digest*, 476, 1995.

[50] **Shih, S., Keir, P. D., Hitt, J., and Wager, J. F.,** *Appl. Phys. Lett.*, 69, 1921, 1996.

[51] **Neyts, K. A. and Corlatan, D.,** *IEEE Trans. Electron Dev.*, ED-45, 768, 1998.

[52] **Grudzinsky, A. S., Keir, P. D., and Wager, J. F.,** *Display and Imaging*, 1999.

[53] **Bouchard, A. F.,** M.S. Thesis, Oregon State University, 1999.

[54] **Peery, J. B.,** M.S. Thesis, Oregon State University, 1997.

[55] **Thuemler, R. L.,** M.S. Thesis, Oregon State University, 1997.

[56] **Davidson, J. D.,** M.S. Thesis, Oregon State University, 1991.

[57] **Davidson, J. D., Wager, J. F., Khormaei, R. I., King, C. N., and Williams, D.,** *IEEE Trans. Electron Devices*, ED-39, 1122, 1992.

[58] **Douglas, A. A. and Wager, J. F.,** *SID 92 Digest*, 356, 1992.

[59] **Douglas, A. A. and Wager, J. F.,** *Electroluminescence*, Singh, V. P. and McClure, J. C., Eds., Cinco Puntos Press, El Paso, TX, 1992, 387.

[60] **Douglas, A. A.,** M.S. Thesis, Oregon State University, 1993.

[61] **Keir, P. D. and Wager, J. F.,** *SID 96 Digest*, 305, 1996.

[62] **Keir, P. D., Le, H., Thuemler, R. L., Hitt, J., and Wager, J. F.,** *Appl. Phys. Lett.*, 69, 2421, 1996.

[63] **Choma, J.,** *Electrical Networks: Theory and Analysis*, Krieger Publishing Co., Malabar, FL, 1991.

[64] **DeCarlo, R. C.,** *Linear Systems*, Prentice Hall, Englewood Cliffs, NJ, 1989.

[65] **Vincent, G., Chantre, A., and Bois, D.,** *J. Appl. Phys.*, 50, 5484, 1979.

[66] **Rosencher, E., Mosser, V., Vincent, G.** *Phys. Rev. B*, 29, 1135, 1984.

[67] **Ando, M., and Ono, Y.,** *J. Appl. Phys.*, 65, 3290, 1989.

[68] **Ando, M., and Ono, Y.,** *J. Appl. Phys.*, 68, 3578, 1990.

[69] **Baukol, B. A., Hitt, J. C., Keir, P. D., and Wager, J. F.,** *Appl. Phys. Lett.*, 76, 185 (2000).

[70] **Hitt, J. C.,** M.S. Thesis, Oregon State University, 1997.

[71] **I. Lee, S. Pennathur, K. Streicher, T. K. Plant, J. F. Wager, P. Vogl, and S. M. Goodnick,** *Inst. Phys. Conf. Ser.*, 145, 1229, 1995.

[72] **N. Abrikosov, V. Bankina, L. Poretskaya, L. Shelimova, and E. Shudnova,** *Semiconducting II-VI, IV-VI, and V-VI Compounds*. Plenum Press, New York, 1969.